

Development of a deflectometry defect detection system

Francisco Matos Gomes Cardoso Afonso

Master Dissertation

FEUP Supervisor: Prof. Pedro Sousa

FEUP Co-supervisor: Prof. Paulo Tavares



Master's in mechanical engineering

September 2022

Resumo

Esta dissertação apresenta o desenvolvimento e montagem de um protótipo capaz de executar ensaios de deflectometria com recurso a apenas uma imagem projetada sobre um objeto, denominada neste projeto de sistema *Single-shot deflectometry*.

A primeira fase deste projeto prendeu-se com uma pesquisa compreensiva de diferentes métodos de metrologia ótica e as suas respetivas vantagens e desvantagens, foi dada especial atenção aos métodos PMD (*Phase Measuring Deflectometry*), ou de deflectometria de medição de fase e os seus respetivos elementos, visto que o método que se procura implementar nesta dissertação pertence a este grupo. Entre os diferentes elementos essenciais ao bom funcionamento de um sistema de deflectometria, foram abordados:

- Configuração dos elementos do sistema;
- Imagens de luz estruturada;
- Desmodulação das imagens capturadas;
- *Unwrapping* da informação transmitida pela fase;
- Integração de declives;
- Calibração do sistema.

Posteriormente foi realizado o desenvolvimento da solução mecânica, envolvendo o projeto e modelação tridimensional de 4 peças auxiliares necessárias ao bom funcionamento do sistema, que foram desenhadas em SolidWorks 2020 e a sua impressão com recurso a filamento PETG. Em paralelo com o desenvolvimento das peças mecânicas foi efetuada a montagem da solução eletrónica, englobando a implementação do circuito eletrónico do motor passo a passo responsável pelo posicionamento angular da peça a ser testada, em relação à câmara, assim como a escrita do *firmware* deste componente com recurso ao ambiente de desenvolvimento integrado Arduino IDE.

Seguidamente, foi verificado que o algoritmo de pós-processamento de imagem fornecido funcionava incorretamente, portanto, foi adotado como objetivo o desenvolvimento de um novo algoritmo de pós-processamento de imagem que apresentasse os mesmos resultados que o anterior se propunha a apresentar, a informação de fase *unwrapped*, que permite a identificação de defeitos na superfície do objeto. Desta forma, o algoritmo de pós-processamento de imagem desenvolvido neste projeto não executa a integração dos declives e, portanto, a reconstrução tridimensional da superfície do objeto em análise. Adicionalmente, com o objetivo de melhorar o funcionamento do algoritmo em relação ao método aplicado no algoritmo anterior, a desmodulação foi implementada segundo o método descrito por Tavares e Vaz (2006), e o método de *unwrapping* da informação transportada pela fase foi mudado para ser compatível com a nova técnica de desmodulação.

Por fim, foi realizada a montagem do sistema e o seu respetivo teste em ambiente controlado. Tendo em conta a geometria do objeto a ser analisado, duas diferentes configurações de montagem do sistema são possíveis, cada uma dedicada a obter imagens de uma determinada área da superfície do objeto. Foram efetuados dois tipos de testes, um a uma imagem contendo um defeito e outro a uma imagem sem defeito superficial, adicionalmente, mais testes foram efetuados de forma a se determinar a influência do contributo do utilizador durante o processo de desmodulação da imagem. Na fase final deste projeto todos estes resultados foram comparados e analisados.

Dos resultados obtidos durante os testes efetuados ao sistema de *Single-shot deflectometry*, é possível concluir que o protótipo desenvolvido atingiu todos os objetivos propostos apresentando uma boa maneabilidade do objeto a ser analisado e um algoritmo de pós-processamento de imagem capaz de apresentar defeitos na superfície do objeto. No entanto, o resultado final está dependente da qualidade da imagem capturada e da experiência do utilizador durante o seu pós-processamento.

Abstract

This dissertation presents the development and assembly of a prototype for performing deflectometry based defect detection using a single image projected onto the object under test, referred to in this project as the Single-shot deflectometry system.

The initial phase of this project concerned a comprehensive research of different optical metrology methods related to deflectometry and their respective advantages and disadvantages. Special attention was given to Phase Measuring Deflectometry (PMD) methods and their respective elements. Among the different essential elements to the proper functioning of a deflectometry system, the following were addressed:

- Configuration of the system elements;
- Structured light imaging;
- Demodulation of the captured images;
- Unwrapping the phase information;
- Slope integration;
- System calibration.

Subsequently, the mechanical solution was developed, involving the design and three-dimensional modeling of 4 auxiliary parts necessary for the proper functioning of the system, which were designed in SolidWorks 2020 and printed using PETG filament. In parallel with the development of the mechanical parts, the electronic solution was assembled, including the implementation of the stepper motor electronic circuit responsible for the angular positioning of the object to be tested, in relation to the camera, as well as writing the firmware of this component using the integrated development environment Arduino IDE.

Next, it was verified that the provided image post-processing algorithm worked incorrectly, therefore, a goal was adopted to develop a new image post-processing algorithm that would present the same results that the previous one was intended to present, the unwrapped phase information, which allows the identification of defects on the surface of the object. Thus, the image post-processing algorithm developed in this project does not perform slope integration and, therefore, the three-dimensional reconstruction of the surface of the object under analysis still requires a final inclination correction. Additionally, with the goal of improving the algorithm in relation to the method applied in the previous algorithm, the demodulation was implemented according to the method described by Tavares and Vaz (2006), and the method of phase unwrapping was changed, in order to be compatible with the new demodulation technique.

Finally, the system was assembled and tested in a controlled environment. Considering the geometry of the object to be analyzed, two different mounting configurations of the system are possible, each dedicated to obtaining images of a certain area of the object's surface. Two types of tests were performed, one within a defective object and the second on a similar surface without defects. Additionally, further tests were performed to determine the influence of the user input during the image demodulation process. In the final phase of this project all these results were compared and analyzed.

From the results obtained during the tests performed on the Single-shot deflectometry system, it is possible to conclude that the developed prototype reached all the proposed objectives, presenting a good maneuverability of the object to be analyzed and an image post-processing algorithm capable of clearly presenting defects on the object's surface, depending on the quality of the captured image and the user's contribution during post-processing.

Acknowledgements

I would like to thank both my dissertation supervisor and co-supervisor, Eng. Pedro Sousa and Dr. Paulo Tavares for allowing me the opportunity to develop this project and learn more about the subject of optics, as well as for their unfaltering support and guidance throughout the entire dissertation.

Thanks to all the UMAI partners that I was able to work with, who helped me develop this project.

My deepest thanks to my family, especially my parents Fernando Afonso and Fátima Afonso, for their support, help and all else they have given me which allowed me to be here in the first place.

Thanks to my other half and future wife Raquel Teixeira for being a loyal and trusting companion throughout this phase of my life.

And finally, I would like to thank my very good friends Pedro Leite and Raúl Silva, for all their help and friendship all these years that we studied together. Our friendship is something that has deeply touched me, and I will always cherish for the rest of my life.

Content

Resumo	iii
Abstract.....	iv
Acknowledgements	v
Abbreviations	viii
Figure Index.....	ix
Table Index	x
1. Introduction	1
1.1. Project framing and motivation	1
1.2. Project objectives and approach.....	2
1.3. Dissertation structure	2
2. State of the art	5
2.1. Specular surface optical metrology.....	6
2.2. Phase Measuring Deflectometry.....	8
2.2.1. System setup	11
2.2.2. Fringes	11
2.2.3. Demodulation.....	13
2.2.4. Phase unwrapping.....	14
2.2.5. Slope integration	15
2.2.6. Calibration	16
3. Single-shot deflectometry	17
3.1. Methodology.....	17
3.2. Components	18
3.2.1. Hardware.....	18
3.2.2. Printed components.....	19
3.3. Stepper motor control	21
3.3.1. Electronic circuit.....	21
3.3.2. Firmware	22
3.4. Image post processing.....	23
3.4.1. Demodulation.....	23
3.4.2. Phase unwrapping.....	27
4. System validation	31
4.1. System setup and calibration.....	31
4.1.1. Object under test	31
4.2. Tests description	33

4.3.	Single-shot results	36
4.4.	Brief discussion.....	38
5.	Conclusion and future projects.....	41
5.1.	Conclusion	41
5.2.	Future projects	42
	Annexes	43
	Annex A: Cross-fringe pattern	44
	Annex B: IDS Camera data sheet (IDS Imaging Development Systems GmbH, n.d.)	45
	Annex C: Stepper motor list (Motion Control Products LTD, n.d.).....	47
	Annex D: Stepper motor base technical drawing	48
	Annex E: Stepper motor casing technical drawing	49
	Annex F: M4 brass threaded inserts specifications (RS Pro, n.d.).....	50
	Annex G: Motor incliner technical drawing	51
	Annex H: Object stand technical drawing	52
	Annex I: Cylindrical protrusion technical drawing	53
	Annex J: Arduino NANO electrical connections (HK Shan Hai Group Limited, n.d.)	54
	Annex K: Stepper motor firmware	55
	References	58

Abbreviations

CCD: Charged Coupled Device

CMM: Coordinate Measuring Machine

CMOS: Complementary Metal Oxide Semiconductor

DC: Dead Center

DFT: Discrete Fourier Transform

FEUP: Faculdade de Engenharia da Universidade do Porto

FFT: Fast Fourier Transform

INEGI: Instituto de Ciência e Inovação em Engenharia Mecânica e Engenharia Industrial

IWFT: Inverse Windowed Fourier Transform

LCD: Liquid Crystal Display

PETG: Polyethylene terephthalate glycol

PMD: Phase Measuring Deflectometry

QGPU: Quality Guided Phase Unwrapping

RGB: Red, Green, Blue

SUT: Surface Under Test

TFT: Thin Film Transistor

UMAI: Unidade de Monitorização Avançada e Integridade Estrutural

WFF: Windowed Fourier Filtering

WFT: Windowed Fourier Transform

Figure Index

Figure 1 - Three-dimensional shape metrology subdivisions.....	6
Figure 2 - Path of light through a Michelson interferometer (Wang et al, 2012).....	7
Figure 3 - Reconstruction of two images with switched phase and amplitude (Tavares, 2008).	8
Figure 4 - Law of reflection (adapted from Huang et al, 2018).	9
Figure 5 - PMD image processing steps.	10
Figure 6 - Height-slope ambiguity problem (Huang et al, 2018).	10
Figure 7 - Approaches to solving the height-slope ambiguity: (a) monoscopic with shifted screens, (b) monoscopic with a point distance sensor, (c) stereoscopic, (d) multi-cameras serving multiple screens (Huang et al, 2018).	11
Figure 8 - Cross-fringe pattern.	12
Figure 9 - Color fringe decomposition into three fringe patterns (Zhang et al, 2017).	12
Figure 10 - Diagram of the different elements of the deflectometry system.....	17
Figure 11 - Hardware components: (a) laptop PC (specifically as a monitor), (b) camera, (c) stepper motor.	18
Figure 12 - Stepper motor base: (a) top view, (b) bottom view.	19
Figure 13 - Stepper motor casing: (a) top view, (b) bottom view, (c) stepper motor base and casing assembled around the stepper motor.	20
Figure 14 - Motor incliners: (a) the printed component, (b) motor incliners angling the motor.	20
Figure 15 - Object stand: (a) top view, (b) bottom view.	21
Figure 16 - Electronic circuit diagram.....	22
Figure 17 - Diagram of the demodulation process.	26
Figure 18 - Comparison between the spatial spectrum and the frequency spectrum of the same image (Adapted from Fisher et al, 2003).....	26
Figure 19 - Comparison between fringe images and their shifted Fourier Transforms.	27
Figure 20 - Steps of a quality guided phase unwrapping method: (a) wrapped phase data, (b) unwrapping path, (c) quality map, (d) unwrapped phase data (Zhao et al, 2011).....	28
Figure 21 - Representation of spatial unwrapping (Zhao et al, 2011).	29
Figure 22 - Single-shot deflectometry system assembly.	31
Figure 23 - Object to be evaluated.....	32
Figure 24 - Object's main areas of interest.....	32
Figure 25 - Captured image of the object reflecting the cross-fringe pattern.....	33
Figure 26 - Post-processing algorithm command window (MATLAB).	34
Figure 27 - Selection of the area to be processed by the algorithm (MATLAB).....	34
Figure 28 - Selection of the cross-fringe frequencies in the frequency domain (MATLAB). .	35
Figure 29 - Wrapped and unwrapped phase data (MATLAB).....	36
Figure 30 - Captured image of object without surface defect.	36
Figure 31 - Results of both tests (Unwrapped phase data).	37
Figure 32 - Unwrapped phase data depending on the crop window.	37

Table Index

Table 1 - Performance of different types of fringe patterns (Zhang et al, 2017).....	13
Table 2 - TMC2209 driver specifications (Biqu, n.d.)	23

1. Introduction

The present dissertation presents the design and assembly of a deflectometry system prototype, which requires a single image of the Surface Under Test (SUT), henceforth referred to as Single-shot deflectometry, as well as the development of necessary firmware for its control and rewriting the image post processing algorithm. Since the previously existing image post processing algorithm contained unidentified issues, it was rewritten and improved. In the interest of further understanding the image post processing techniques, the rewriting of this algorithm became one of the main objectives of the thesis work. This deflectometry system was then tested on an object with a specular surface.

Metrology methods have grown significantly in importance over time, as evidenced by the study conducted by Huke *et al* (2014) attesting the importance of nondestructive testing of objects as the basis of quality control in a production line, indicating a range of tactile and optical methods for detection of surface defects, as well as other methods for the detection of subsurface defects. For the latter, optical methods such as thermography and interferometry can also be used in combination with an applied load.

Specifically, vision-based optical defect detection techniques are the main focus of this paper. These methods are widely used in quality control and in turn, directly affect customer satisfaction, production cost and profitability. Recently, these optical methods have enjoyed higher implementation in quality control for a vast range of products such as aluminum sheets, locomotive trails, liquid crystal displays (LCD), plastic objects, sphere parts, agricultural food produce, fabric and textile industry, among others (Akhtar *et al*, 2019).

Similarly, in the review conducted by Huang *et al* (2018), quantitative three-dimensional shape metrology is mentioned to have become a staple for quality control, reverse engineering, precision manufacturing and artwork digitalization. Zhang *et al* (2017) correlate the development of integrated circuits, photovoltaics, the automobile industry, advanced manufacturing, and astronomy to the need of obtaining three-dimensional shape data of objects fast and accurately, for applications of quality control and function evaluation.

The project conducted by Akhtar *et al* (2019) is an example of the implementation of optical metrology methods for the quality control of a product. This project implemented the Phase Shifting Deflectometry method with the use of a robotic arm carrying a screen and camera setup. This system would scan the surface of various automobile parts, detecting surface defects. Implementing this system results in the elimination of an expensive, labor intensive and highly subjective manual visual inspection process which often produces inconsistencies, translating in the overall decline of productivity and quality.

As evidenced, the need to obtain accurate three-dimensional shape measurements has grown to a point where metrology methods have become a staple in several industries. This dissertation, along with its objectives, also aims at analyzing the importance of metrology methods and conduct a brief review of different types of metrology techniques, with a special focus on optical techniques, and deflectometry, which will be implemented in this project.

1.1. Project framing and motivation

This project's theme conforms with the investigation carried out at the Advanced Monitoring and Structural Integrity Unit (UMAI – Unidade de Monitorização Avançada e Integridade Estrutural), of INEGI (Instituto de Ciência e Inovação em Engenharia Mecânica e Engenharia Industrial). INEGI, along with FEUP (Faculdade de Engenharia da Universidade do Porto), the Engineering College of Porto University, have proposed this theme for a master's degree thesis in the area of automation.

The UMAI Optics Laboratory was made available, along with its resources and the guidance of Professor Pedro Sousa and Professor Paulo Tavares as the supervisor and co-supervisor, respectively, of the present thesis.

The Advanced Monitoring and Structural Integrity Unit of INEGI specifically targets the development of monitoring, structural condition and non-destructive inspection systems with

or without contact, and solutions which may be applied for the evaluation of structural conditions as well as predictive maintenance.

Considering the projects undertaken by this unit, the current work aims to develop a fast, non-destructive optic method which can be used in quality control of several types of products.

Personally, as a future automation mechanical engineer, I was motivated to participate in this project taking into consideration the opportunity to develop a system which integrates the areas of mechanical project, electronic systems, programming, and image processing. It is also motivating to be able to contribute to INEGI's portfolio and the unit in which I am conducting this research.

1.2. Project objectives and approach

This project aims to conclude several requirements, to be achieved by the end of the thesis work, which are:

- A comprehensive analysis of the state of the art regarding non-destructive optical methods, specifically deflectometry
- 3D modeling and design of the deflectometry system
- Implementation of the electronic circuit allowing control of the deflectometry system
- Assembly of the deflectometry system
- Rewriting of the deflectometry image processing algorithm
- Testing of the developed system

The 3D modelling and design of the deflectometry system will be executed using SolidWorks. It is expected that the resulting system, combined with the very light weight of the subject under analysis will allow for the 3D printing of the geometry using Prusament PETG filament.

The necessary circuit schematics to control the stepper motor were provided and assembled using a breadboard. This stepper motor will, in turn, be integrated into the system and enable the control of the specimen's position, thereby providing the ability to execute the deflectometry analysis at various angles, its firmware will be written using Arduino IDE.

The deflectometry system is then to be assembled in an optical table using M6 screws, in a controlled area, limiting the ambient light to avoid its interference in the trials.

Finally, the deflectometry image processing algorithm will be written using MATLAB R2021a.

1.3. Dissertation structure

The dissertation is subdivided into 5 main chapters, as follows:

Chapter 1: Introduction (this chapter). A general introduction to the theme of this thesis is made in this chapter, analyzing the importance of metrology and its application in today's industry. The existing problem is exposed, along with the approach taken to solve it. All the entities and people involved in this project are introduced. The motivation and objectives for the execution of this academic project are presented.

Chapter 2: State of the art. The second chapter goes over the different types of optical metrology methods, their differences and respective advantages and disadvantages. Special consideration is given to the deflectometry method, scrutinizing its different types and implementations, studies developed on this subject as well as the different phases of its execution.

Chapter 3: Single-shot deflectometry. The design, construction, and assembly of the system, as well as its circuitry and firmware are presented in this chapter. The deflectometry image processing algorithm is introduced.

Chapter 4: System Validation. The developed system is put to the test in practical trials within a controlled environment, where the results are analyzed.

Chapter 5: Conclusion and future projects. The obtained results are listed and analyzed, several possible improvements for the final project are conceived and suggested to be implemented in future iterations of this prototype.

2. State of the art

As explained above, the field of three-dimensional shape metrology has grown to a point where it has established itself as a much-needed necessity in many different industries. However, this also entails that a vast number of different techniques have been developed and attempting to describe every single profilometry method would be beyond the scope of the present dissertation.

Many different factors must be considered when determining which method is more suited to a certain application, such as whether the type of surface is specular or diffuse, if it is a contact method or not, the field of vision in optical methods, among others. These parameters also enable labelling these methods, but unfortunately the number of different techniques is vast, as stated before, making this a daunting task.

Nevertheless, most three-dimensional shape metrology techniques, can be subdivided into contact or contactless methods, depending on whether they require contact between the sensor and the object under test, or not. Contact-based profilometry methods exhibit high resolution, with measurements in the order of nanometers. Some contact-based methods include stylus profilometer, scanning tunneling microscopy, scanning force microscopy and coordinate measuring machine (CMM). These techniques are independent of surface characteristics or the scanned geometry and can function well in dirty environments. However, since they require contact, some products sensible to touch may be damaged during measurement, and their operating speed is also slow. Therefore, these methods are not advisable to fragile and sensible surfaces, such as paint finished parts and lenses, or operations that require fast measurements. (Akhtar *et al*, 2019).

On the other hand, non-contact profilometry methods can perform fast surface scanning as well as its three-dimensional reconstruction. The applicability of these methods depends on the type of surface of the object since specular surfaces may prove difficult to measure. Therefore, in this case, in order to make the object behave like a diffuse surface it might be necessary to coat it. Coating certain objects, however, may prove impossible due to its fragility or other factors. These non-contact techniques depend on the nonuniform reflection of light from the surface of an object, caused by defects, and should be prioritized for applications where fast readings are necessary. However, since it is dependent on the object's surface, dirt or dust will affect measurements and its results (Akhtar *et al*, 2019). As stated by Akhtar *et al* (2019), some non-contact methods include common structured light projection (Xu *et al*, 2017), phase shifting interferometry (Groot, 2011), deflectometry (Maldonado *et al*, 2014) and digital holographic microscopy (Kim, 2010).

Optical three-dimensional shape metrology is one of the most important metrology techniques, widely used today, including for the inspection of high-quality surfaces (Huang *et al*, 2018). Since in the present work the author aims to implement the deflectometry technique, which is an optical metrology method, special consideration will be given to these types of techniques.

According to the review conducted by Huang *et al* (2018), optical methods can further be subdivided according to their field of view. Depending on this parameter, the methods may resort to pointwise scanning, line-by-line scanning or even full-field vision-based measurement.

Pointwise scanning techniques must scan the surface of the object to be measured, dividing it in very small areas or even pixel by pixel (Tiziani and Uhde, 1994), while line-by-line scanning techniques scan "slices" of the object's surface (Xi *et al*, 1999). On the other hand, full-field methods afford a larger field of vision, usually a two-dimensional plane of the surface.

Interestingly, Huang *et al* (2018) also found out when comparing pointwise scanning deflectometry to full-field PMD (Phase Measuring Deflectometry), that while full-field methods exhibited lower precision than pointwise methods, they are faster and their field of view and dynamic range are much easier to adjust, depending on the application for the method.

Full-field methods can, in turn, as evidenced by the research conducted by Tavares (2008), have another subdivision depending on whether they are active or passive. Passive methods involve the measurement of radiation present in the object, while active methods require interaction between the object to be evaluated and the method setup, usually light is employed for this interaction.

Passive image sensing techniques depend on visual cues such as accommodation, convergence, binocular disparity or motion parallax to determine depth perception. Photogrammetry, structure from motion, shape from shading and photometric stereo being some of the few most used approaches to these types of techniques. As for the active image scanning techniques, there are many prominent methods such as single point and laser scanners, slit scanners, time-of-flight, Moiré methods, pattern or structured light projection and coded structured light (Tavares, 2008).

All the subdivisions described above can be visualized in Figure 1, since a deflectometric method will be implemented in the present project, the path highlighted by the continuous line indicates which subdivisions apply to this particular chosen technique.

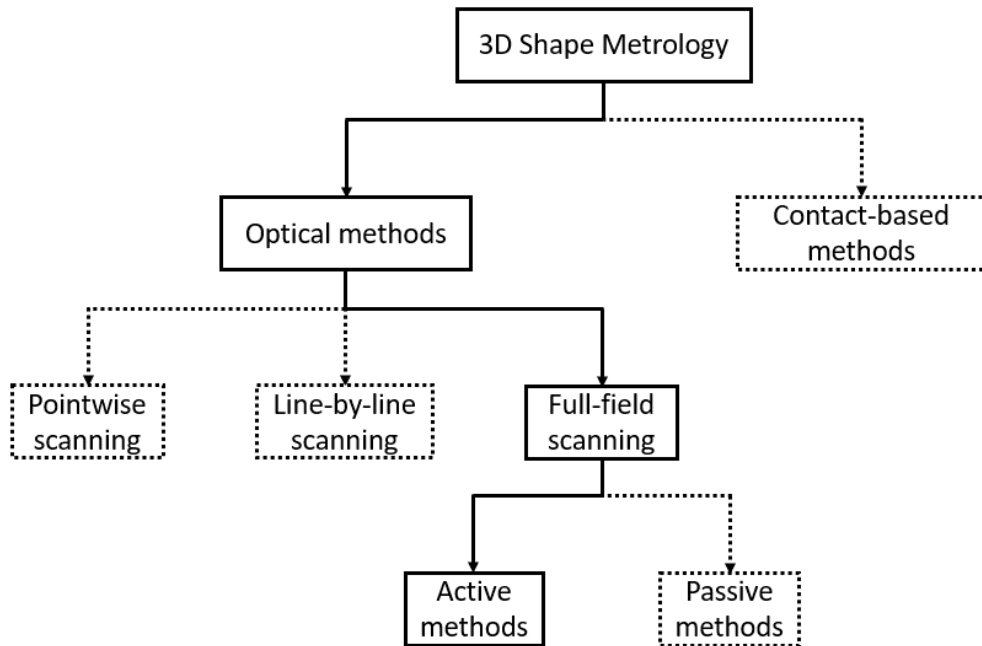


Figure 1 - Three-dimensional shape metrology subdivisions.

2.1. Specular surface optical metrology

As mentioned before, the optical measurement of surfaces is highly dependent on the type of surface, the measurement of specular surfaces is often still a challenge, owing to the surface's reflective quality. As researched by Zhang *et al* (2017), when it comes to the case of specular surface measurement, there are three main types of methods that are usually employed:

- Common Structured Light Projection
- Interferometry
- Deflectometry

As further indicated by both Zhang *et al* (2017) and Akhtar *et al* (2019), usually, for a measurement of a specular surface to take place, it must be sprayed with a powder spray, this happens because image saturation problems due to total reflection in parts of the surface may occur in the measurement of glossy or reflecting surfaces, making it necessary to apply a matte coating for it to behave like a diffuse surface. After applying the coating on the specular surface, a common structured light projection technique may be used for the measurement, such as in the project developed and published by Xu *et al* (2017), where a full-field fringe pattern projection profilometry was implemented. This preparation is not necessary and therefore not applied to deflectometry.

Unfortunately, the use of coatings may influence the geometry of the surface and depending on the type of coating used different results may be achieved, while other objects such as antiques and sensible equipment such as certain optical components should not be sprayed (Zhang *et al*,

2017). A study conducted by Palousek *et al* (2015) analyzes the effect of matte coating on objects, when it comes to the accuracy of three-dimensional optical measuring techniques, by comparing a chalk coating and a titanium coating when measured by a structured light projection scanner. Titanium matte coating performed better than the chalk matte coating, being much thinner than the latter and presenting an uncertainty of $0.44\ \mu\text{m}$ while chalk coating exhibited an uncertainty of $3.9\ \mu\text{m}$ in repeated tests.

Interferometry, as described by Sansoni *et al* (2009), works by projecting, onto an object's surface, a periodic pattern that varies spatially or temporally, superimposing the reflected light with a predetermined reference pattern. The resulting interferometric pattern from the superposition of reference and object beams can be used to demodulate the signal carried through the reflected light, and thereby calculate surface geometry. The result exhibits very high resolution and control, microprofilometry and surface quality control being one of the most common applications of this technology. Zhang *et al* (2017) and Akhtar *et al* (2019) both confirm the high accuracy of these types of methods, however, they should be implemented when measuring simple surfaces such as spheres, planes, and weakly aspheric surfaces, since a reference pattern is needed for these methods to successfully function, it is difficult to measure aspheric mirrors or even free-form specular objects using interferometry. In addition, the field of view is restricted, complicating its use for large surfaces and the use of interferometric methods outside of controlled laboratory settings may prove too challenging, due to the nature of the method and the presence of uncontrollable noise sources. In summary, interferometry is not suitable for the measurement of highly curved or large surfaces.

The workings of a Michelson interferometer are displayed in Figure 2, where the aforementioned description can better be visualized.

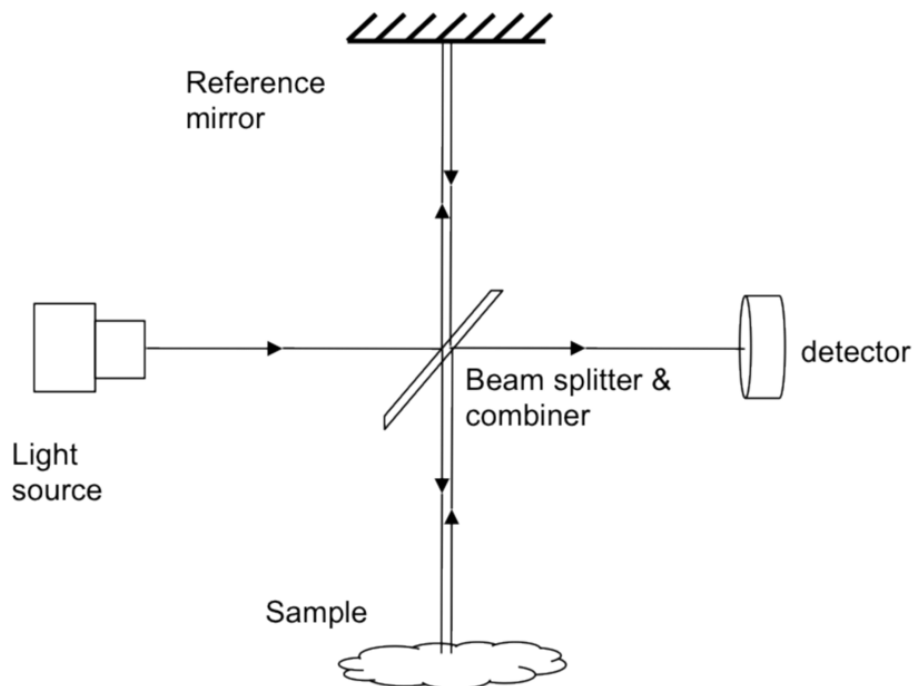


Figure 2 - Path of light through a Michelson interferometer (Wang *et al*, 2012).

Zhang *et al* (2017) found that while deflectometry, in some ways overcomes the shortcomings of interferometry, reconstructing the surface is often a challenge. To measure specular surfaces with steep slopes and large sizes, deflectometry methods have been researched and developed, leading to many diverse types of deflectometry techniques, some of which being (Zhang *et al*, 2017):

- Moiré deflectometry
- Ronchi method
- Phase-measuring deflectometry (PMD)
- Laser scanning techniques

Legarda-Saenz (2007) describes Moiré deflectometry as a technique to measure the deflection of light rays when travelling through a phase object. This method is based on the Moiré and Talbot effects and its setup requires a collimated light source and two Ronchi gratings separated along the light beam axis. A Moiré pattern, also known as a deflectogram is formed when superimposing the shadow of the front Ronchi grating by projecting it onto the Ronchi grating located further back. The object under analysis is placed in front of the light beam, modifying the Moiré pattern on account of the ray deflections produced by optical properties of the object itself. As identified by the study conducted by Wang *et al* (1999), there exist many approaches to process and evaluate the Moiré deflectograms, such as the intensity measuring method, automatic fringe detecting method and electronic heterodyne read-out method, all these methods exhibit moderate accuracy.

Royo (1999) describes the Ronchi method as using a light source to project light into a concave surface, additionally, a Ronchi grating is placed in the path of the converging reflected light. Behind the Ronchi grating a detector is placed, so the resulting deformed or straight shadows of the fringes in the grating can be analyzed. The standard setup for this method measures the transverse ray aberration in two orthogonal directions at the location where the Ronchi grating is placed, obtaining the wavefront aberrations and slopes on the surface that is being measured.

An example of the implementation of laser scanning deflectometry can be found in the work developed by Ishikawa (2014), where a high-accuracy autocollimator is moved horizontally while scanning a surface. This device is able to return the surface profile, and in the case of this study, the repeatability (average standard deviation) was less than 4 nm.

2.2. Phase Measuring Deflectometry

Since the objective is to analyze an object's surface using a single image, which might require a large field of view, and seeing as the base for the new code, the previous algorithm, was meant for a PMD implementation, the working principle of this project will also be Phase Measuring Deflectometry. This subsection focuses on the different variations of this method.

As stated by Tavares (2008), the information carried by the phase is, in many ways important to the formation of an image, to the point where the use of the phase information marks the difference between coherent and incoherent image formation. In Figure 3, a curious demonstration is made by Tavares (2008) where phase and intensity of images were compared, and while intensity also carries information regarding the image, in some situations phase information may be regarded as more prominent.

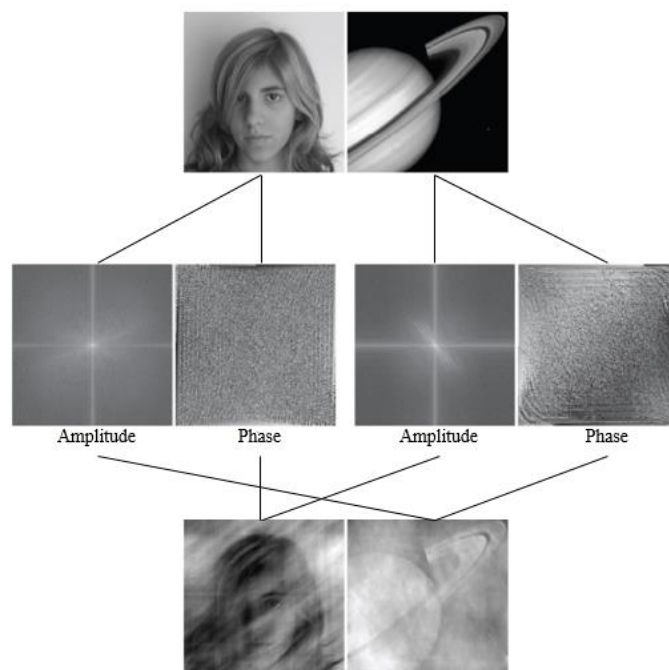


Figure 3 - Reconstruction of two images with switched phase and amplitude (Tavares, 2008).

In the demonstration, the complex phase and amplitudes of two images were switched and reconstructed. From the resulting images it is concluded that retaining phase information results in an understandable image reconstruction, while the amplitude does not.

To better understand the importance of phase for three-dimensional surface reconstruction, we can describe it as the difference between a two-dimensional image and a three-dimensional hologram. The hologram can keep the object and reference wave fields phase and intensity, carrying its information, and therefore is able to display it in three dimensions (Tavares, 2008).

As demonstrated, it is expected that the phase of an image reflected by the object under test carries highly accurate data regarding the objects surface. In this regard, many variations of phase-measuring deflectometry (PMD) methods have been researched. These methods, implemented for their ability to measure specular objects, also benefit from a large dynamic range, being a non-contact operation, having a full-field field of view and automatic data processing (Zhang *et al*, 2017).

PMD is a structured light full-field active method, it was first developed by Horneber *et al* (2000) and over time it was improved to be able to measure different specular objects. This method can also be used on semi-specular objects for defect detection (Akhtar *et al*, 2019).

Zhang *et al* (2017) describes the classical PMD method as follows. Initially, sinusoidal fringe patterns are generated digitally and projected (by means of a digital screen) onto the surface to be measured. From another point of view, the reflected fringes will be deformed, on account of the surface slopes, and are recorded using an imaging device such as a CCD (Charged Coupled Device) or CMOS (Complementary Metal Oxide Semiconductor) camera.

The principle behind the setup of this method is the law of reflection. As is illustrated in Figure 4, a change in the slope of the surface of α degrees from position A to position B translates into a change of 2α on the reflected ray of light, a consequence of a fundamental fact respecting reflection whereby a ray of light reflects at the exact same angle to the surface normal direction. Usually, for better understanding, the ray of light is considered to originate in the camera (Huang *et al*, 2018).

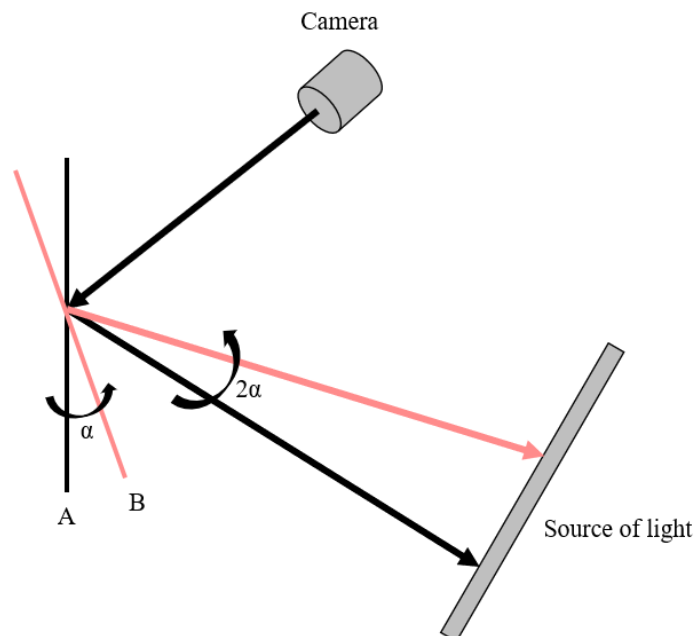


Figure 4 - Law of reflection (adapted from Huang *et al*, 2018).

Unwrapped phase data can then be obtained by shifting or stepping the pattern projected onto the surface of the object through 3 or 4 steps and using the captured images in a phase shifting algorithm. Subsequently, this data is unwrapped to obtain the absolute phase data, which is used to calculate the slope of the surface, using the system parameters, and then integrated to reconstruct the three-dimensional surface (Zhang *et al*, 2017). The steps depicting the process after the attainment of the deformed fringe image can be visualized in Figure 5.

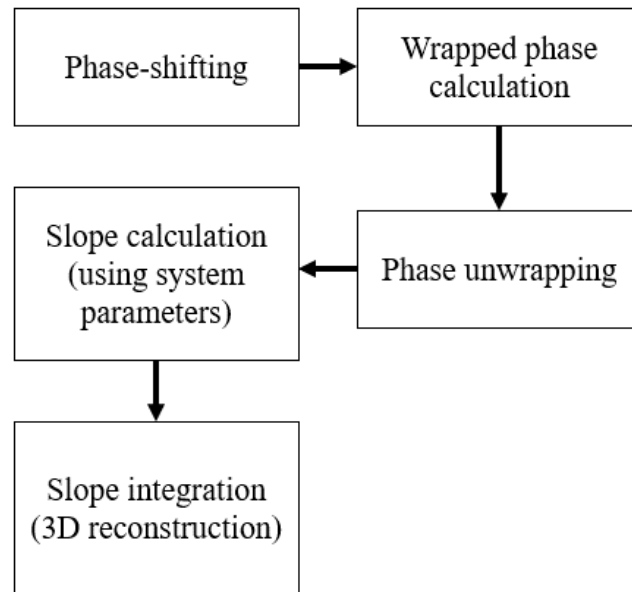


Figure 5 - PMD image processing steps.

One challenge of the PMD method is known as the height-slope ambiguity, as we can see in Figure 6, there are many different possibilities for the height and slope of the elements in the system. Their positions are important to implement the geometric calibration of the system, which is used in the final steps of the image processing procedure, to reconstruct the three-dimensional surface. Since there are many different combinations possible, the system does not know the global position of its components.

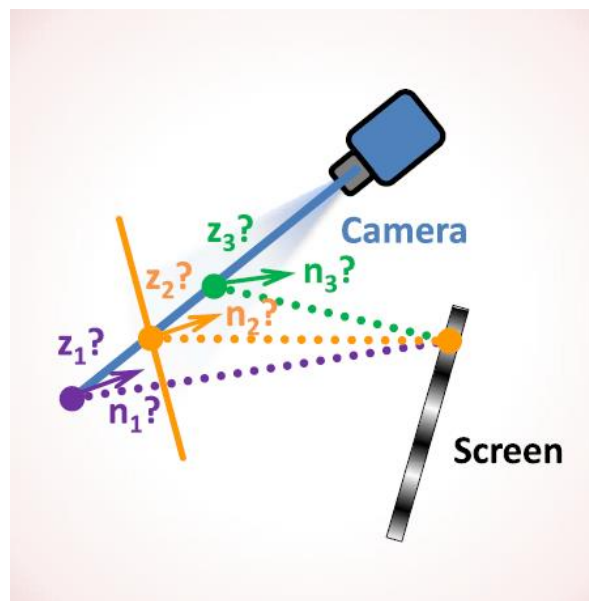


Figure 6 - Height-slope ambiguity problem (Huang et al, 2018).

The use of two cameras (stereo-camera PMD) can simplify the geometric calibration of the deflectometry system, in fact, PMD allows for the use of more than two cameras in a system (multi-camera), however, multi-camera systems are rarely used owing to the fact that at one point the reflected ray is oriented in a certain direction, and this ray can only be captured, theoretically, from this certain direction, making it difficult to include multiple cameras in a single system. For this reason, PMD systems usually employ one or two cameras. It's also of note that most problems with using this method come from measuring objects with discontinuities or isolated surfaces (Zhang *et al*, 2017).

2.2.1. System setup

Huang *et al* (2018) identifies several PMD systems according to their setup, that is, the number of cameras or screens present. Most commonly, these systems are:

- Monoscopic
- Monoscopic with shifted screens
- Monoscopic with a point distance sensor
- Stereoscopic
- Multi-camera with several pairs of screens and cameras

A representation of these systems can be seen in Figure 7. These setups present different approaches to help solve the height-slope ambiguity problem by allowing the system to know its components relative position, usually with the introduction of another component (such as a camera). In the case of the monoscopic with shifted screens approach in Figure 7(a), the reflected ray is determined by two or more points of intersection on the shifted screen. In Figure 7(b), the monoscopic approach with a point distance sensor is represented, solving the height-slope ambiguity problem by providing a distance value. The remaining approaches (Figure 7(c) and Figure 7(d)) both try to solve the ambiguity by reducing the discrepancies of the normal vectors calculated for the object's surface by each of the cameras, and in this way describe height values (Huang *et al*, 2018).

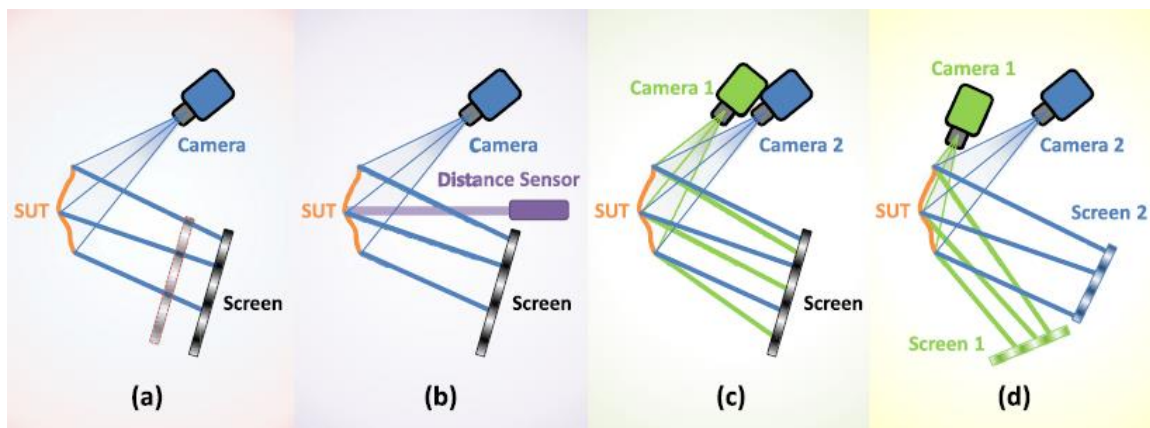


Figure 7 - Approaches to solving the height-slope ambiguity: (a) monoscopic with shifted screens, (b) monoscopic with a point distance sensor, (c) stereoscopic, (d) multi-cameras serving multiple screens (Huang *et al*, 2018).

2.2.2. Fringes

This subsection deals with the different types of fringes that constitute the structured light to be projected onto the object under test. The present subsection was based on the research developed by Zhang *et al* (2017), which indicates that two local slope data's need to be integrated to reconstruct the surface three-dimensionally. Usually this is obtained by displaying vertical and horizontal fringes sequentially (such as in phase-shifting deflectometry), however, this method is slower because it demands the capture of the sequential fringe patterns, complicating the implementation of this method in dynamic systems. To answer this problem, cross-fringe and color fringe patterns have been researched (Zhang *et al*, 2017).

Orthogonal Fringe Pattern

Horizontal and vertical patterns are generated digitally and subsequently projected, in sequence. Researchers usually display two sets of patterns, one of horizontal fringes, and the other of

vertical fringes. These fringes are reflected, deformed by the SUT, captured and used for image post processing (Zhang et al, 2017).

Cross-fringe Pattern

To avoid sequentially displaying a set of images, resulting in slower testing, cross-fringe patterns were researched (Figure 8). These patterns simultaneously display both horizontal and vertical fringes in a single image, reducing the time needed to complete the process, allowing this method to more easily be implemented in dynamic systems (Zhang et al, 2017).

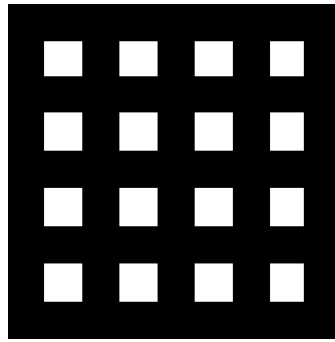


Figure 8 - Cross-fringe pattern.

Using Fourier fringe analysis, this results in vertical and horizontal wrapped phase data, which can be subsequently unwrapped, making it possible to measure the surface of a specular object using only one cross-fringe pattern (Zhang et al, 2017).

Color Fringe Pattern

The development of color cameras allowed for the research of color fringes which can be even faster than binary cross-fringes, color encoded fringe projection techniques are used today to measure dynamic objects, this approach can be used in PMD, provided the use of a color LCD and camera (Zhang et al, 2017).

With a phase shift of $-2\pi/3$, 0 and $2\pi/3$, fringe patterns are coded into the red, green and blue (RGB) channels creating the color fringe. From the processing of the reflected color fringe images, three fringe patterns can be extracted, as shown in Figure 9. If cross-fringes are applied to color fringes it is possible to retrieve six fringe patterns from only one color image (Zhang et al, 2017).

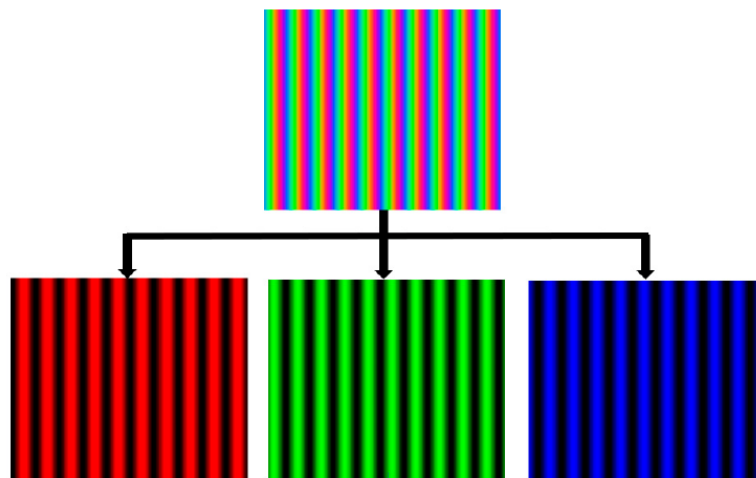


Figure 9 - Color fringe decomposition into three fringe patterns (Zhang et al, 2017).

Zhang *et al* (2017) grouped their findings comparing these three fringe methods in terms of time (duration), accuracy and resolution. These results can be seen in Table 1 (Zhang *et al*, 2017).

Table 1 - Performance of different types of fringe patterns (Zhang *et al*, 2017)

	Orthogonal Fringe	Cross-fringe	Color Fringe
Time	Long	Short	Shortest
Accuracy	High	Median	Low
Resolution	High	Median	High

2.2.3. Demodulation

The demodulation of captured images results in the wrapped phase data, necessary for further image post processing. According to Huang *et al* (2018), depending on the required number of frames, demodulation methods can be divided into:

- Single-frame methods
- Multiple-frame methods

Huang *et al* (2018) further describe single-frame methods as only requiring one frame to be able to calculate phase data. These usually include transform-based methods such as Windowed Fourier Transform (WFT). Two directional phase values are required to calculate slopes in the vertical and horizontal directions, therefore a cross-fringe pattern is used in this example to carry this information in a single frame.

The captured image of the fringes display an intensity which can be described by (Huang *et al*, 2018):

$$I_{(x,y)} = a(x,y) + b_x(x,y) * \cos[\phi_x(x,y)] + b_y * \cos [\phi_y(x,y)] \quad (1)$$

Where:

x and y are the screen orthogonal coordinates

a(x,y) is the background

b_x(x,y) and b_y(x,y) are the modulations of x and y directional sinusoidal fringes

ϕ_x(x,y) and ϕ_y(x,y) are the fringe phases in the horizontal and vertical directions

Finally, the wrapped phases of the horizontal and vertical fringes can be retrieved as shown in equations 2 and 3 (Huang *et al*, 2018):

$$\phi_x^\omega(x,y) = \arctan \frac{\text{Im}[\bar{f}_x(x,y)]}{\text{Re}[\bar{f}_x(x,y)]} \quad (2)$$

$$\phi_y^\omega(x,y) = \arctan \frac{\text{Im}[\bar{f}_y(x,y)]}{\text{Re}[\bar{f}_y(x,y)]} \quad (3)$$

Where:

$\bar{f}_x(x,y)$ and $\bar{f}_y(x,y)$ represent the filtered x and y directional exponential fringe patterns

The same article published by Huang *et al* (2018) proceeds by describing multiple-frame methods as using several phase-shifted fringe images, requiring a method such as phase-shifting deflectometry. In this case, the fringe pattern is described by equation 4 (Huang *et al*, 2018):

$$I_n(x,y) = a(x,y) + b(x,y) * \cos \left[\phi(x,y) + \frac{2n\pi}{N} \right], n = 0, 1, 2, \dots, N - 1 \quad (4)$$

Where:

a(x,y) is the background

$b(x,y)$ is the modulation of x (horizontal) or y (vertical) fringes

$\phi(x,y)$ is the phase of x (horizontal) or y (vertical) fringes

While the wrapped phase can be calculated using (Huang *et al.*, 2018):

$$\phi^\omega(x, y) = -\arctan \frac{\sum_{n=0}^{N-1} I_n \sin(\frac{2n\pi}{N})}{\sum_{n=0}^{N-1} I_n \cos(\frac{2n\pi}{N})} \quad (5)$$

An interesting technique is described by Tavares and Vaz (2006), where a two-dimensional Fourier Transform is applied to the reflected fringe image. The Fourier logarithmic spectrum contains two frequency peaks when centered at the carrier frequency (one regarding the vertical fringes, and the other regarding the horizontal fringes). To obtain the horizontal and vertical slope data, carried by these fringes, their respective frequencies are isolated, in the Fourier logarithmic spectrum. This is done by applying a window around each of these frequencies. The algorithm then moves the windows to the center of the spectrum, where an inverse Fourier transform is applied, effectively isolating the frequencies and their phase information. While simple, this method is prone to mistakes, this technique was further improved in the article written by Tavares and Vaz (2013), where problems regarding the elimination of the zero-frequency peak were addressed.

After the fringe demodulation, the phase data is wrapped in the interval $[-\pi, \pi]$. To be able to further continue processing the image it is necessary to unwrap these values.

2.2.4. Phase unwrapping

The phase value is related to temporal or spatial wavelengths, and it lies between $[-\pi, \pi]$ radians. Because these values are limited, they are referred to as wrapped and relate to unwrapped phase through (Tavares, 2008):

$$\phi(x, y) = \psi(x, y) + 2\pi n(x, y) \quad (6)$$

Where:

ψ is the unwrapped phase

ϕ is the wrapped phase

Therefore, to use the phase data to reconstruct the surface three-dimensionally it is necessary to unwrap the phase values, extending them beyond the limit $[-\pi, \pi]$ in which they come after the demodulation process. In the context of three-dimensional surface metrology, the unwrapping process requires a low noise phase map, otherwise phase discontinuities may appear, significantly complicating this process (Tavares, 2008).

In the thesis published by Tavares (2008), phase unwrapping is subdivided into:

- Path-following techniques
- Full-field methods

Path-following techniques integrate phase while following a predetermined path (which can depend, or not, on the data). As described previously, the main challenge regarding phase unwrapping are discontinuities, which seem to stem from steep shape changes, aliasing, or noise corrupted gradients. The success rate of path-following unwrapping techniques is directly correlated to the path chosen (unless a way to avoid inconsistent data is implemented into the procedure itself). Some path-following methods are (Ghiglia and Pritt, 1998):

- Linear Scanning
- Spiral scanning
- Pixel Queuing
- Region Scanning
- Branch Cutting
- Quality-Guided methods

- Mask-Cutting
- Flynn's Minimum Discontinuity
- Cellular Automata

On the other hand, full-field methods calculate phase independently for every pixel by processing the entire image at once. Some generally accepted techniques for this type of unwrapping method are (Tavares, 2008):

- Minimum-Norm methods
- Deterministic phase unwrapping
- Temporal phase unwrapping

Another interesting path-following method frequently used for phase unwrapping is an algorithm described in the article by Kemaio (2007). This method is based on the Windowed Fourier Transform and includes denoising of the image prior to the phase unwrapping phase, this is necessary since noise can ruin the results of this algorithm that analyzes the image line by line. The fringe patterns are transformed into its Windowed Fourier Transform spectrum, and since noise permeates the whole spectrum, it can be filtered, before applying an inverse Windowed Fourier Transform to obtain a smooth image (Kemaio, 2007).

2.2.5. Slope integration

Once the absolute phase data is obtained, their locations on the image can be determined using the known parameter of the pattern fringe's period. The global coordinates for the intersection points of the structured light rays on the screen can also be determined, thanks to the geometric calibration (Huang *et al*, 2018).

For every pixel, the normalized vector of the emitted light ray is determined by camera calibration, subtracting the coordinates of the reflected ray vector to the emitted ray vector results in the surface normal vector (equation 7). The horizontal slopes can, in turn, be calculated by dividing the x coordinate of the normal vector, by its z coordinate (equation 8), and the vertical slopes can, similarly be calculated by dividing the y coordinate of the normal vector by the z coordinate (equation 9), these values allow for the three-dimensionally reconstruction of the surface (Huang *et al*, 2018).

$$N = r - e = (N_x, N_y, N_z) \quad (7)$$

Where:

r is the vector representing the reflected light ray

e is the vector representing the emitted light ray

N is the surface normal vector

$$s_x = -\frac{N_x}{N_z} \quad (8)$$

$$s_y = -\frac{N_y}{N_z} \quad (9)$$

Where:

s_x represents the horizontal slopes

s_y represents the vertical slopes

With the resulting data, the slopes can be integrated to reconstruct the surface. Huang *et al* (2018) indicate that there exist three main categories of reconstruction methods:

- Zonal reconstruction
- Modal reconstruction
- Piecewise reconstruction

Zonal reconstruction methods apply finite differences of height along both the horizontal and vertical directions to be able to establish values between slopes with unknown height. Modal reconstruction methods use analytical models and finally, piecewise reconstruction methods use radial basis functions, working subset by subset since it requires a lot of memory usage (Huang *et al*, 2018).

2.2.6. Calibration

Calibration is one of the most common procedures in metrology processes, in this case it can be subdivided into geometric calibration and camera calibration.

Geometric calibration

To integrate the slope data and obtain the reconstructed three-dimensional surface, it is required to accurately calibrate the system parameters. Geometric calibration tracks the optical ray reflection in a global coordinate system where the other components, such as the LCD (light source) the camera and the object are present, their position being known.

This process involves identifying the positions of the camera, screen, and object on the desired coordinate system, however this often proves quite challenging since the screen is outside the field of view of the camera. It is common to use a planar mirror to reflect the LCD screen, allowing the camera to observe the reflected image of the screen (Zhang *et al*, 2017).

As published by Zhang *et al* (2017), most geometric calibration methods can be subdivided into three categories:

- A plane mirror with markers;
- A plane mirror;
- An auxiliary device or moving device.

Camera calibration

Camera calibration establishes internal parameters, such as focal length, principal point coordinates and image radial and tangential distortion coefficients (Zhang *et al*, 2017).

Quite a few other studies have proposed different approaches when it comes to the camera calibration. Tsai (1987) gathered and classified a collection of camera calibration methods before presenting their own two-step technique which displayed more consistent results. A more recent review of camera calibration techniques has also been published by Salvi *et al* (2002). Zhang (2000) proposed what was to become a popular camera calibration method using a checkered plane, this technique requires only that the system camera observe a planar pattern from a few orientations (recommended at least four or five different orientations to obtain better quality). This method is quite flexible when considering that classical techniques require expensive equipment such as two or three orthogonal planes.

3. Single-shot deflectometry

The third chapter of this dissertation presents the work developed to fulfill three of the main objectives of this project, these objectives being the 3D modeling and design of the Single-shot deflectometry system, the implementation of the electronic circuit for the control of the system, and the development and improvement of the image processing algorithm. More specifically, the type of method chosen, its setup, components, and final image processing will be detailed.

3.1. Methodology

The required method for the project is deflectometry, therefore a simple monoscopic setup was adopted since, compared to other setups, it is cheaper and easier to implement. The original image processing algorithm did not reconstruct the three-dimensional surface of the measured object, focusing only on the detection of defects, which can be done after the unwrapping process and obtaining the absolute phase data. The improvements aimed to be achieved in this work do not include the three-dimensional reconstruction of the object's surface either and therefore, camera calibration or a detailed geometric calibration, which sets the parameters necessary for slope integration, for which other setups such as a stereoscopic setup are better suited, will not be required. A cross-fringe pattern (Annex A) was chosen to achieve the analysis of a surface using only one frame, this choice has the potential to reduce image processing time when compared with the commonly implemented phase-shifting technique, that requires the analysis of several images. As for the demodulation process, the method described in detail and tested by Tavares and Vaz (2006) was implemented, since it displayed good results. When compared to the original algorithm's code this constitutes an improvement, which is discussed in higher detail in subsection 3.4.1. As the final step of the image processing algorithm, the phase unwrapping was implemented using an adapted version of the algorithm presented in the work developed by Kemao (2007), also differing from the original image processing algorithm.

All the different components that integrate this system work together, as can be observed in Figure 10, where the different interactions between these components are represented. A computer is necessary to generate the cross-fringe pattern on its display and subsequently project it onto the object. At this point, the operator must give instructions to the positioning system through the controller firmware, on which the object is mounted. While moving it, the object's position can be discerned through the camera's software (IDS peak Cockpit) which displays the images observed by the camera in the setup. When the surface to be evaluated is visible in the camera software and the intended surface is illuminated by the cross-fringe, the fringe reflection off its surface will be captured manually and stored in the same computer where the post processing algorithm will analyze the image.

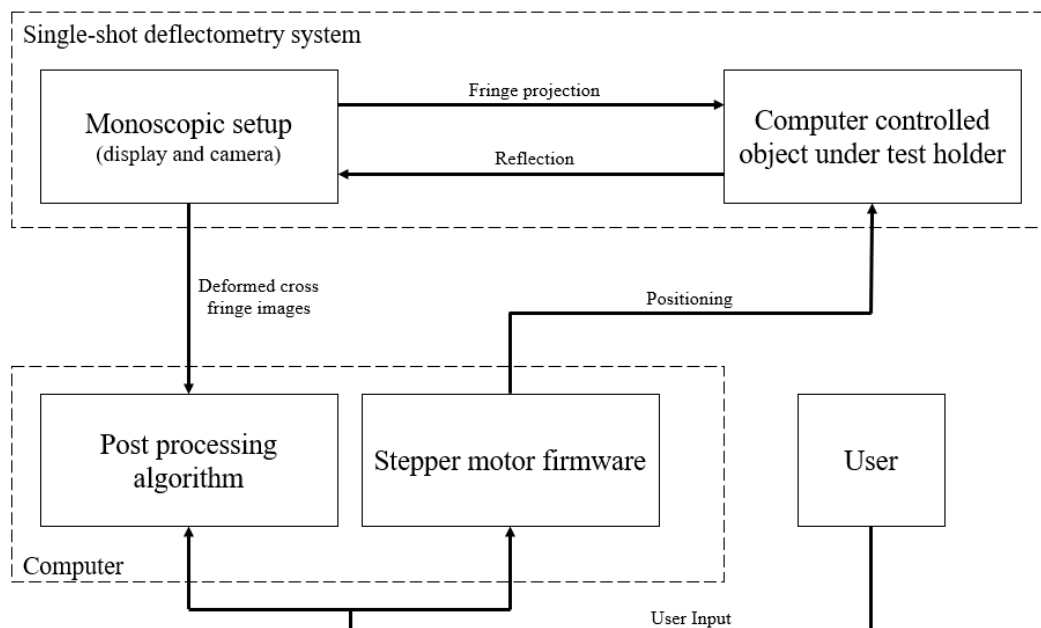


Figure 10 - Diagram of the different elements of the deflectometry system.

3.2. Components

All the components that integrate the Single-shot deflectometry system are hereby presented. These include one laptop computer monitor, one CMOS camera, one stepper motor and five 3D printed components.

3.2.1. Hardware

Laptop Monitor

The monitor used belongs to the laptop computer Asus Eee PC (Seashell series) with 1024x600 pixel resolution and a 10.10 inch display with a 16:10 aspect ratio. The computer displays a cross-fringe generated image onto the object under analysis.

The monitor's position and inclination on the optical table was established iteratively, where it was determined that the display would need to be angled relative to the table. This was one of the main reasons why this component was chosen, since it provides a screen with a high degree of rotation, allowing it to easily be tilted to the desired position.

Camera

The camera used for the Single-shot deflectometry system is a UI-3370CP-M-GL Rev.2, commercialized by IDS Imaging Development Systems GmbH. Additionally, the lens used was a Linos MeVis-C 25mm f/1.6. As an auxiliary component to the camera, a tripod was used to secure the camera's position and angle. The camera's data sheet can be accessed in Annex B.

Stepper motor

The employed stepper motor is the model M42STH47-1684S, commercialized by Motion Control Products. This motor can function with a six-wire connection or a four-wire connection and further details about this component can be seen in Annex C (where the chosen model is highlighted in red).

To aid in the functioning of this component, four printed parts were designed, two of them with the purpose of encasing the motor and assuring its immobilization in the optical table, another one to establish an angle to the motor, subsequently tilting the object, and a final component to display the object under test.

In Figure 11 all the presented hardware components are visible.

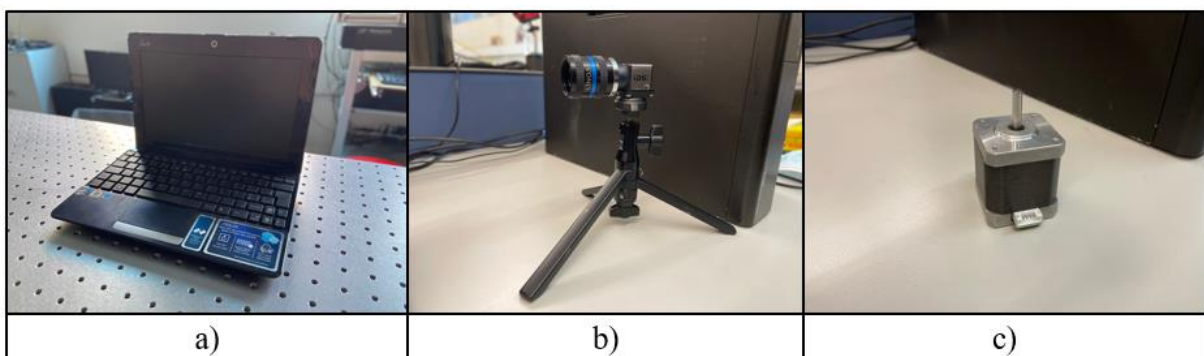


Figure 11 - Hardware components: (a) laptop PC (specifically as a monitor), (b) camera, (c) stepper motor.

3.2.2. Printed components

The designed components were printed in an Original Prusa i3 MK3S printer using PETG filament with a 20% infill. Several indications are important when it comes to the three-dimensional printing of components, namely, the geometry of a component may compromise the precision of the printing process, since printing in a horizontal plane away from the printer's base requires material underneath, which may require printing supports. Therefore, the orientation of a component should be carefully considered to prioritize the adequate printing of higher quality details. The different types of printed components are presented in the following subsection.

Stepper motor base

The stepper motor base printed component (Figure 12) encases the lower sides of the motor, allowing the base of the motor to touch the optical table. Through four correctly spaced M6 holes (the optical table possesses threaded M6 holes in a 25mm-by-25mm grid), the printed component allows the insertion of appropriate screws, who attach this part to the optical table. Additionally, the stepper motor base includes five M4 holes, which are used for connection to the stepper motor casing. The technical drawing of this component can be found in Annex D.

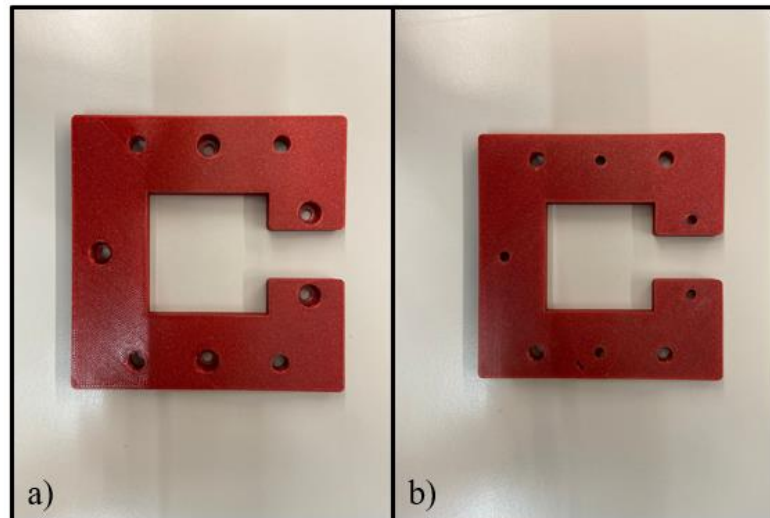


Figure 12 - Stepper motor base: (a) top view, (b) bottom view.

Stepper motor casing

The stepper motor casing shown in Figure 13, as the name suggests, encases most of the motor and is attached to the stepper motor base printed component by means of M4 screws. To this end, M4 brass threaded inserts were inserted into the M4 holes, as is visible in Figure 13(b), enabling the screws to connect the stepper motor casing to the stepper motor base component. Four M3 holes were placed in the upper surface of the printed component, allowing it to be attached to the stepper motor, in addition, a 22.2 mm diameter hole exists to allow the presence of the protrusion around the motor's shaft. A small entrance for the motor wire connections was also included, matching with the entrance designed in the stepper motor base component, this detail is visible in Figure 13(c) where both stepper motor printed components are assembled, along with the stepper motor itself. Annex E contains the technical drawing of this component. Additionally, Annex F contains the details pertaining to the brass threaded inserts used.

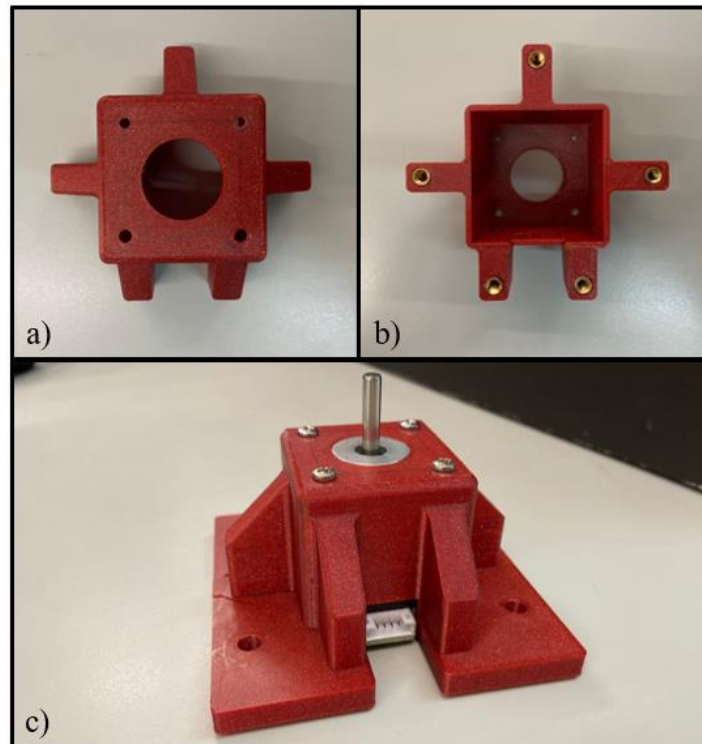


Figure 13 - Stepper motor casing: (a) top view, (b) bottom view, (c) stepper motor base and casing assembled around the stepper motor.

Motor tilting

Because the object's geometry is complex, to better analyze different parts of its geometry, it might be necessary to tilt it differently. Most of the object's surface can be analyzed using the Single-shot deflectometry method in two different angles, one of them being attained by positioning the motor base directly on the optical table (0° of inclination in relation to the optical table), and the other by angling the motor approximately 55° in relation to the optical table. These printed components (Figure 14), hereby named motor incliners, achieve the necessary angling of the motor for the latter situation, which subsequently results in the angling of the object stand and the object itself.

When using this component, the M6 screws previously used to attach the motor base printed component to the optical table, now connect it to the motor incliners, which in turn possess four M6 holes to allow its attachment to the table. Since no threaded inserts existed for the M6 hole size, the holes of the motor incliners used for the screws that connect it to the motor base were printed with thread. The technical drawing for this component can be found in the Annex G.

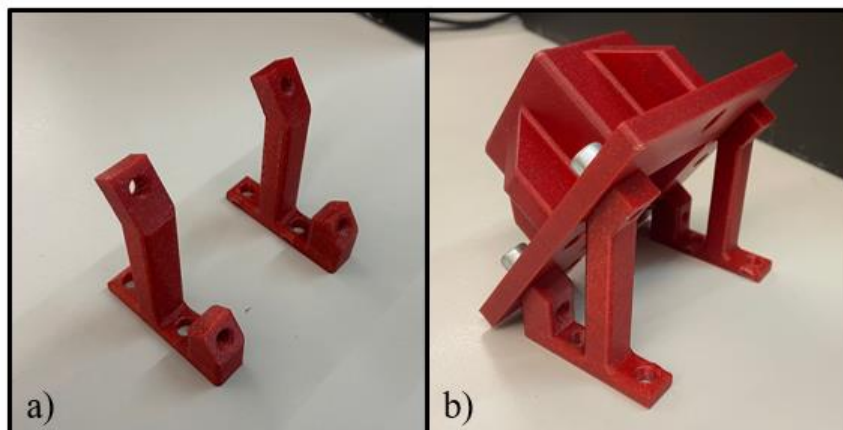


Figure 14 - Motor incliners: (a) the printed component, (b) motor incliners angling the motor.

Object stand

The final printed component is the stand where the object will be fixed. For the analyzed objects, the designed stand is a rectangular table with an indent where the object will be placed. Originally, this rectangular piece had a hole with the shape of the stepper motor shaft, where the motor connected and because of its semi-cylindrical shape, the motion was transferred between the motor, and this printed component. Even though several test parts with different clearances were printed to find the correct size for the shaft shaped hole, after testing, it was confirmed that due to the rotation of the shaft, the hole deformed gradually, enough for the precision of the rotation to visibly worsen.

Therefore, a cylindrical protrusion was designed, this new component can be inserted into the object stand, and to further connect these components, avoiding the gradual deformation of the inside of the object stand's hole, they were glued together. The opposite end of the cylindrical protrusion includes a hole in the shape of the motor's shaft (partially cylindrical), where the shaft enters under pressure, together with an M3 screw, to assure a correct transfer of motion. Figure 15 displays these two printed components already inserted and glued, a brass M3 insert was included on the side (Figure 15(b)), where the screw will press against the shaft, securing it in its place firmly. The technical drawings for both the object stand and the cylindrical protrusion may be consulted in Annex H and I, respectively.

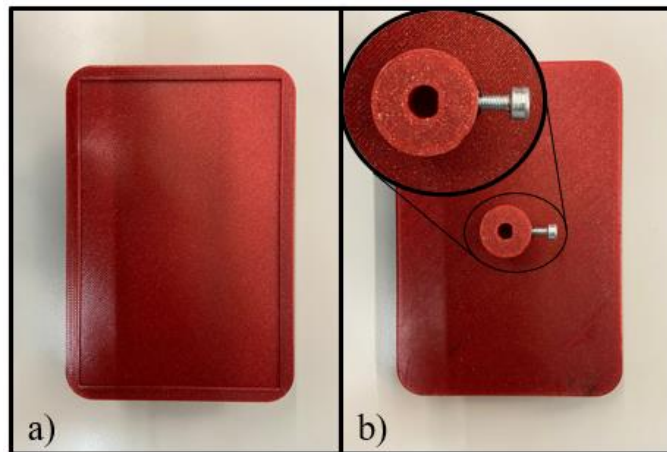


Figure 15 - Object stand: (a) top view, (b) bottom view.

3.3. Stepper motor control

One of the most important parts of the Single-shot deflectometry system is the control of the object's position through the stepper motor firmware, seen before in Figure 10. To achieve this, an electronic circuit was built, and its firmware written.

The present subsection focuses on the necessary steps to make the stepper motor hardware functional.

3.3.1. Electronic circuit

The electronic circuit is composed of many different electronic components, for this application, the used electronic parts are as follows:

- 1 Arduino NANO
- 1 Stepper motor driver (UART BTT TMC2209 V1.2)
- 3 capacitors
- 4 resistors

Figure 16 displays a diagram where the main connections between the different electronic components are presented. The capacitors function as low pass filters, while the resistors were connected in series to form R1. The necessary connections were made to ensure the correct functioning of the microcontroller Arduino NANO, according to this component's data sheet (Annex J). This component communicates with the stepper motor driver via UART communication, which communicates with the computer via Mini-B USB cable.

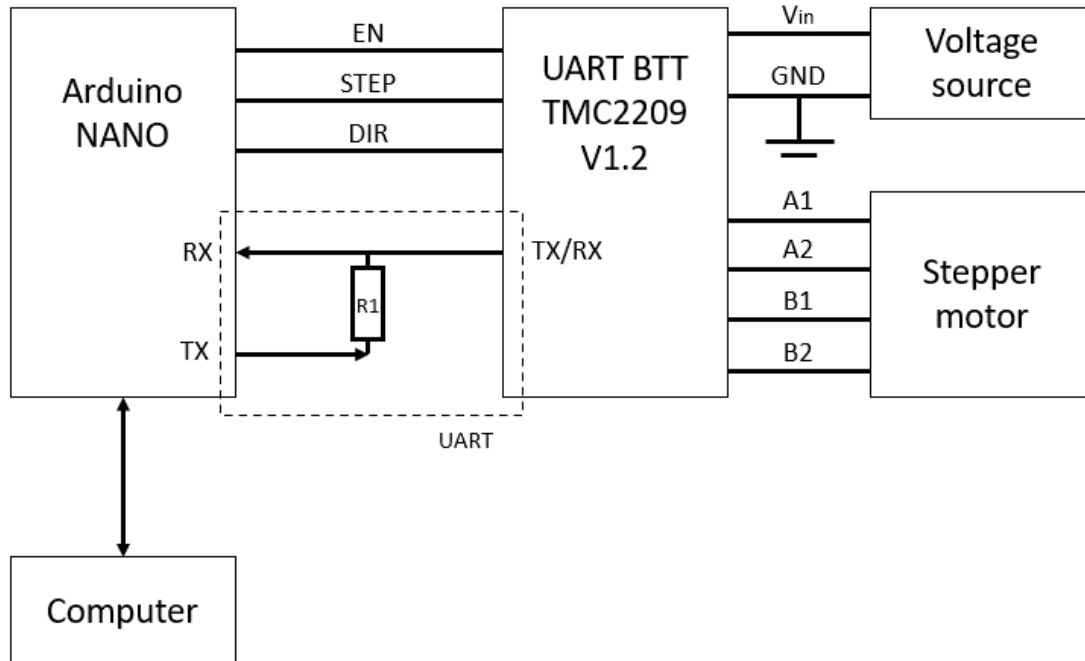


Figure 16 - Electronic circuit diagram.

EN signifies the Enable connection, allowing the motor driver to function, STEP detects an impulse meant to move the motor, DIR determines the direction of the movement, V_{in} is the power input from the voltage source to power the motor and GND is the ground connection. The A1, A2, B1 and B2 connect the driver to the coils of the stepper motor, the A connections being related to one coil and the B connections to the other coil. While the stepper motor itself allows a 6-wire configuration, this setup establishes a 4-wire connection.

As is visible in Figure 16, the user can send instructions to the Arduino microcontroller (via USB), who in turn can transmit and receive information directly to the motor driver (via UART communication or directly through digital signals), as well as determine when and how the motor should move. The stepper motor driver receives the necessary voltage and current from the source and uses it to power the stepper motor suitably, through a 4-wire connection to each of the two coils of the motor.

3.3.2. Firmware

In the writing of the firmware, two libraries were used, the *TMCStepper* and the *SoftwareSerial* libraries. The former is a library publicly available on GitHub, or through the library manager in the Arduino IDE software, that facilitates the control of a stepper motor, for a range of different stepper motor drivers by Trinamic. While the Arduino NANO used already contains two pins dedicated to serial communication, these pins are already used to relay communications between the microcontroller and the computer, therefore, the *SoftwareSerial* library is used to allow serial communications using other digital pins of the microcontroller. These pins will be used for the communication between the Arduino NANO and the motor driver.

Initially, several variables are defined, such as the pins for the software serial communication, the aforementioned EN, DIR and STEP pins, as well as the TX and RX, type of driver, its address and the *rsense* value (sensing resistor), which was determined by Table 2.

Table 2 - TMC2209 driver specifications (Biqu, n.d.)

	TMC2209 Driver
Configuration	CFG Pins or UART
Logic Supply Voltage	3.0 – 5.0 V
Motor Supply Voltage	5.5 – 28.0 V
Maximum Phase Current (RMS)	2.0 A
R _{sense}	110 mOhm

Additionally, the motor RMS current was set to 0.6 A and the motor was controlled using microstepping, to achieve smoother movements. To this end, the microsteps were established as 1/16 of a single normal step.

While using this firmware the user will be able to input one of several commands, each to rotate the object under analysis a certain number of degrees, it is possible to rotate the object 45°, 90°, 180° and 360°. For the object that will be tested, this resolution suffices in clearly displaying its surfaces. Once a rotation of the object is successful, a message is sent to the user, who may now initiate another rotation. A copy of the firmware written for the stepper motor can be found in Annex K.

3.4. Image post processing

The objective of the post processing algorithm is to analyze the phase information carried by the captured deformed fringe images and thus, identify surface defects present in the object under analysis.

As mentioned in Section 1, the original image processing algorithm had significant issues, therefore, in the interest of better understanding image processing methods, this code was rewritten. Some sections of the newly written algorithm differ from the original algorithm, namely the demodulation method, which was improved, and the phase unwrapping technique which had to be changed since the new demodulation method was not compatible with the already existing phase unwrapping technique.

3.4.1. Demodulation

After the image is loaded into the algorithm, it is necessary to demodulate it, as explained in the previous section. This process effectively separates the information carried by the cross-fringe pattern into the vertical fringe information and the horizontal fringe information, in the form of wrapped phase.

The method employed is the demodulation process explained in the article by Tavares and Vaz (2006). This method is based on the Fourier transformation of an image, and it was implemented as follows.

Initially, the image is loaded onto the algorithm, turned into a black and white image, and stored as a matrix. In this case, the used camera for the single-shot system already captures images in black and white. The loaded image is presented to the user where a cropped portion of it may be taken, to focus the image processing on a specific surface area, possibly containing surface defects (this cropped image is the image that will be processed by the algorithm). The cropped image is then stored as another matrix, with its dimensions defined by the number of pixels in the cropped image and its values representing the intensity of each pixel, this method being the standard way of storing images in MATLAB.

At this point, a Fourier transformation is applied to the image matrix, and to better visualize the results, the Fourier transformation is rearranged by shifting the zero-frequency component to the center of the matrix and a logarithmic transformation is applied. The resulting matrix is then represented back as an image, where the phase of the original image is obtained.

The Fourier transform is a tool often used in image processing and can decompose an image into its respective sine and cosine components, giving information regarding its frequency. Every single point in the frequency domain corresponds to a frequency present in the spatial domain. After a Fourier Transform is applied to an image, the result is that very image but in its frequency domain, as opposed to how we usually visualize it, in its spatial domain (Fisher et al, 1996).

Assuming that a certain image is captured from a real-life scenario, in this image's spatial domain the value of each pixel represents the RGB (Red, Green, and Blue) values on that point, additionally, a change in position in that image (in pixels) translates directly to a change in position on the real-life scenario. On the other hand, in that image's frequency domain each point represents a particular frequency contained in the original spatial domain image, and a change in the image position while in the frequency domain represents a change in the spatial frequency of the original image. In addition, a value of a certain point A in this domain can be interpreted as the amount that the intensity in the image varies (spatial frequency) over a certain distance relative to a point in the spatial domain (Fisher et al, 1996).

For example, in a certain image, on the frequency domain, a certain point representing a frequency of 0.1 (corresponding to one period for every ten pixels) has a value of 20. This can be interpreted by understanding that in the spatial domain the intensity values vary over a distance of 10 pixels in relation to a certain point, with a contrast of 40 gray levels ($20 * 2$) between the darkest and lightest intensity values (Fisher et al, 1996).

Several image processing methods use this domain because it better displays periodic relationships in the spatial domain, in truth some image operations are more successful or can only be applied to the frequency domain (Fisher et al, 1996). One such method is the one used in the demodulation of the image post processing algorithm of this project.

When it comes to digital image processing, the Discrete Fourier Transform (DFT) is often used, which is the sampled Fourier Transform and does not contain all the frequencies that form an image. It contains, however, several samples large enough to completely represent the spatial domain image (Fisher et al, 1996).

For a certain image f , applying the DFT results in an image F of the same size, such that:

$$\hat{F}[f] = F \quad (10)$$

$$\hat{F}^{-1}[F] = f \quad (11)$$

Where:

\hat{F} represents the DFT.

\hat{F}^{-1} represents the inverse DFT.

f is the image in the spatial domain.

F is the image in the frequency domain.

As described by Mazet (2021), for a certain image of size $(M \times N)$, the two-dimensional Discrete Fourier Transform is represented by:

$$F(u, v) = \sum_{m=0}^{M-1} \sum_{n=0}^{N-1} f(m, n) * e^{-j*2\pi(\frac{um}{M} + \frac{vn}{N})} \quad (12)$$

Where:

$f(m, n)$ represents the image in the spatial domain.

$e^{-j*2\pi(\frac{um}{M} + \frac{vn}{N})}$ corresponds to the basis function to each point $F(u, v)$ in frequency domain.

Similarly, it is possible to execute the inverse operation, transforming an image in the frequency domain to the spatial domain, using the inverse Fourier transform as written by Mazet (2021):

$$f(k, l) = \frac{1}{M*N} \sum_{u=0}^{M-1} \sum_{v=0}^{N-1} F(u, v) * e^{j*2\pi(\frac{um}{M} + \frac{vn}{N})} \quad (13)$$

Where:

$f(k, l)$ represents the image in the spatial domain.

$e^{-j*2\pi(\frac{um}{M}+\frac{vn}{N})}$ is the basis function to each point $F(u, v)$ in frequency domain.

The result of the Fourier Transform is a complex number, owing to the importance of the information carried by the phase, and since this project aims to implement a phase measuring method, the wrapped phase data must be obtained from this result. This can be achieved by dividing the imaginary component of the result by its real component, as shown in subdivision 2.2.3. (Tavares, 2008).

Some other interesting properties of the DFT, described by Mazet (2021), include:

- It is a periodic function displaying two different periods, M and N:

$$F(u, v) = F(u + kM, v) = F(u, v + lN) = F(u + kM, v + lN) \quad (14)$$

Where:

$$k, l \in \mathbb{Z}$$

- An image translation is represented by a shift on the DFT:

$$F[f(m - m_0, n - n_0)] = F(u, v)e^{-j2\pi(\frac{um_0}{M}+\frac{vn_0}{N})} \quad (15)$$

- If a rotation is applied to the image, the very same rotation will be applied in the DFT.
- A two-dimensional DFT can be calculated by computing the rows and columns separately, using a one-dimensional DFT for each.

The DFT is, however, very demanding to compute, therefore the Fast Fourier Transform (FFT) is applied instead. The FFT is a computationally fast and efficient way of applying the Discrete Fourier Transform, for reference, to compute a one-dimensional DFT algorithm, it would require N^2 multiplications, while the FFT only requires $N * \log(n)$ multiplications (N being the dimension of the data) (Fisher et al, 1996).

As concluded by the article published by Schatzman (1996), discrete Fourier transforms computed using the FFT display far more accurate results than slower transforms, these results, however, are heavily dependent on the type of software used. In the case of the present thesis, the built-in Fast Fourier Transform of MATLAB R2021a was used to convert the original cropped image of the object's surface.

The way the written algorithm demodulates the data to achieve the wrapped phase information follows the diagram of Figure 17.

In the aforementioned description of this process, it is understood that the visualization of both positive and negative spatial frequencies of the FFT require a shift of the magnitude, so that the frequency equaling zero is in the center of the image and the higher frequencies are at its borders, a logarithmic scale is usually employed to better visualize the result. The shifted frequency domain images exhibit symmetry, between points, to the center of the frequency domain image.

At this point, the user will be presented with a clear image of the frequency spectrum where two frequency points will stand out, these correspond to the information carried by both the vertical and horizontal fringes of the cross-fringe, respectively. The user must now manually crop these frequencies by establishing a window around the two different frequency points, these two cropped frequency matrixes will, in turn, be moved to the center of the Fourier spectrum each by being placed in the center of a null matrix of the same size as the original image that was processed by FFT.

From here the logarithmic operation is undone, and the resulting matrixes are unshifted, resulting in two matrixes carrying only the information contained in the relevant frequencies. The phase values can now be calculated for each of the elements of matrixes, resulting in two final matrixes each contain the wrapped phase information for the horizontal and vertical deformed fringes, respectively.

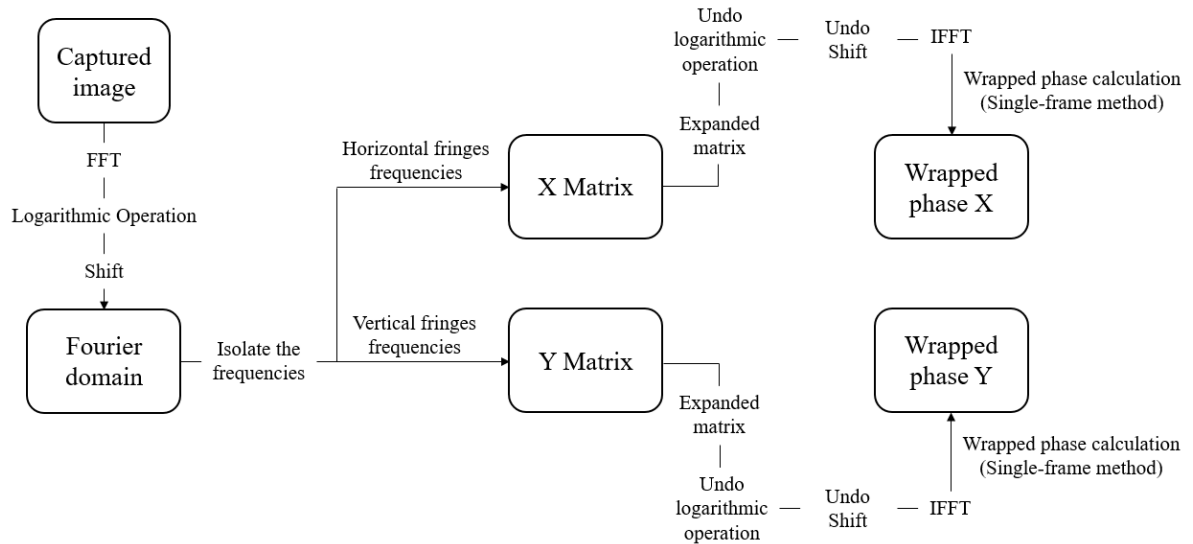


Figure 17 - Diagram of the demodulation process.

Since the correct identification of the surface defects depends on the ability of the user to correctly interpret the frequency domain images, it is also important to establish how to better understand the images in this spectrum.

As an example, in Figure 18 the same black and white picture can be observed in the spatial domain and in the frequency domain, following the described process. As can be discerned, the DC (Dead Center) value, corresponding to the center of the image is without doubt the biggest element, on the other hand, for higher frequencies the value heavily decreases, therefore, in this example, the lower frequencies contain more information than the higher frequencies (Fisher et al, 1996).

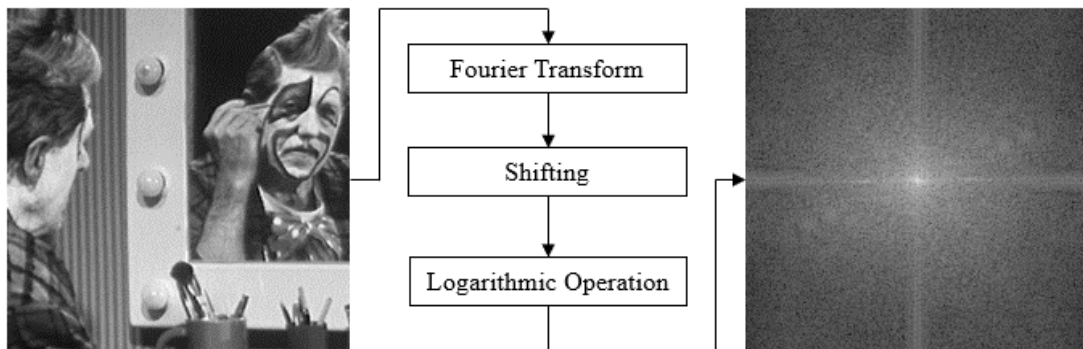


Figure 18 - Comparison between the spatial spectrum and the frequency spectrum of the same image (Adapted from Fisher et al, 2003).

Furthermore, two lines pass through the center, indicating two dominant directions in the image, lines like these are created based on the geometric patterns of the image in the spatial domain (Fisher et al, 1996).

In Figure 19 some simpler examples are detailed, where we can see the clear distinction between the different types of fringes and their respective shifted Fourier Transforms. The Fourier Transform images in Figure 19 haven't undergone the logarithmic application, however, for simple designs such as the ones presented, the results are clearly visible.

Taking as an example the set of images a), three values are observable, the DC value and two symmetrical values about the centered origin representing the positive and negative values of the original spatial frequency. It is interesting to notice that the number of pixels between the symmetrical values and the origin is the same as the number of fringes on the image in the spatial domain. Since the image in the Fourier representation, or its frequency spectrum is symmetrical to its center, two different points represent the frequency of the fringe pattern

image on the left. As expected, when comparing the different images between each other, it is apparent that the higher the frequency of the fringes, the further from the center the values are, also, a rotation of the fringes translates into the very same rotation on the frequency spectrum, as indicated before. As observed, the rotation of the points in the frequency domain follows the direction in which the intensity of the pixels changes the most in the spatial domain image.

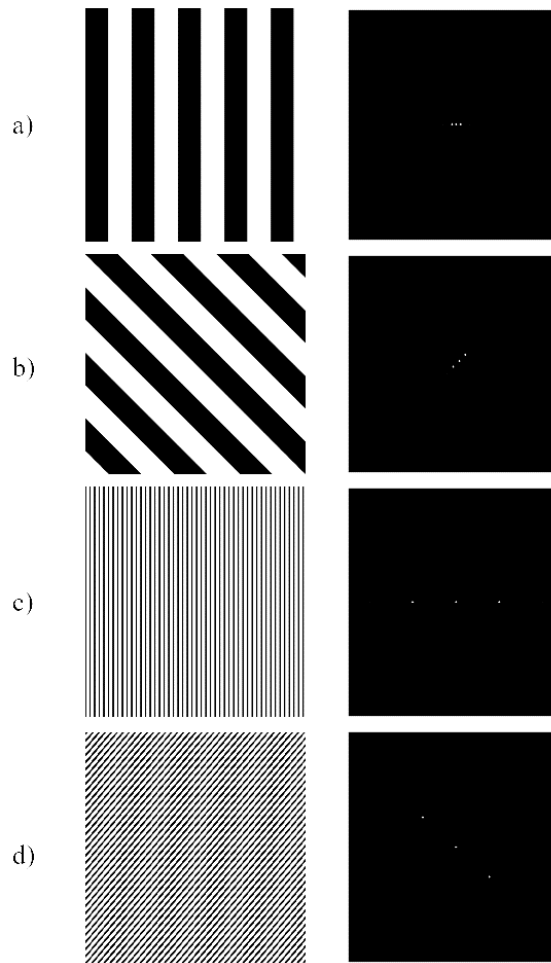


Figure 19 - Comparison between fringe images and their shifted Fourier Transforms.

Overall, the demodulation process differs from the original image processing algorithm since it only applied a mask around the vertical and horizontal directions that cross the center, in the frequency domain, effectively including the vertical and horizontal frequencies in this mask and then representing them separately. However, depending on the case, the thickness of the mask could prove to not be enough when encasing the necessary frequencies, or the opposite, having a mask too thick and not optimal. Since the mask was applied automatically, there was no way of adjusting it for each case. With the method implemented in the rewritten algorithm, the mask is applied by the user, when cropping the relevant frequencies, therefore optimizing this process.

3.4.2. Phase unwrapping

At this point in the algorithm, the wrapped phase values of the deformed fringes are stored in the two resulting matrixes. To visualize the final images, it is necessary to unwrap these results.

The obtained wrapped phase is constrained between the range $[-\pi, \pi]$ radians, this means that every time the phase value is outside of this range, its value is increased or decreased by a factor of 2π in addition with the actual phase value. Therefore, phase unwrapping is an essential step in obtaining the final images.

The method chosen to unwrap the phase data is an adaptation of the algorithm presented in the article written by Kemao (2007), introduced in subsection 2.2.4. In his work, Kemao (2007) develops two algorithms based on the Windowed Fourier Transform (WFT), one of which the Windowed Fourier Filtering (WFF), that can also be implemented for the process of phase unwrapping.

The WFT and its inverse transformation (IWFT) are two transformations which, similarly to the previously analyzed FFT, can deconstruct an image into a frequency spectrum and reconstruct it back into the spatial spectrum, respectively. The WFT utilizes a different base function than the FFT, resulting in a series of blocks, which scrutinize the fringe images. The resulting frequency domain image gives information on the frequency at each pixel of the image, however, the computational cost of the WFT is heavy (Kemao, 2007).

To effectively unwrap the phase information, different techniques can be employed as described before in subsection 2.2.4. Quite often a linear method is employed where the phase map is analyzed by the algorithm, as the name implies, line by line, while simultaneously compensating the $[-\pi, \pi]$ intervals, however, one main concern with using linear methods is their poor performance when applied to a noisy wrapped phase map. The WFF transformation applies a filter that smooths the image and removes unwanted randomly dispersed noise, making it a good solution for the phase unwrapping section of the algorithm, since it can remove possible noise in the wrapped phase map, afterwards, the phase unwrapping can be easily computed (Kemao, 2007).

In this project, the WFF is used to first filter the wrapped phase data, allowing for easier unwrapping which will be executed by a path-finding method, more specifically, a quality guided phase unwrapping algorithm, developed by Qian Kemao.

Thanks to the work developed and published by Zhao et al (2011), the way quality guided phase unwrapping methods (QGPU) work can be observed. As an example, in Figure 20 the several stages of a QGPU algorithm can be found, Figure 20(a) is the wrapped phase data, who by following the quality map (Figure 20(b)) and a path (Figure 20(c)) can be unwrapped (Figure 20(d)). The presented unwrapping path is very detailed with the purpose of displaying the efficiency of QGPU methods, as for the quality map, the lighter colors (light yellow) represent pixels with higher quality, that will be unwrapped first and the darker colors (dark red) are the pixels with the worst quality that will be processed last. In this type of methods, the quality map and the guiding path are of extreme importance to the success of the process.

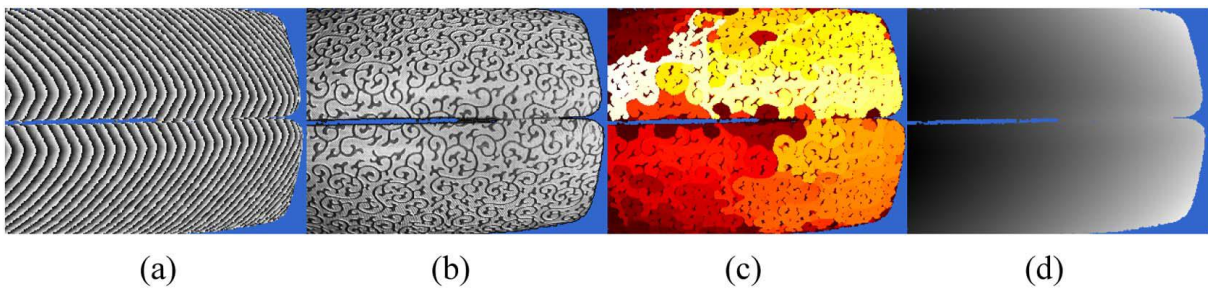


Figure 20 - Steps of a quality guided phase unwrapping method: (a) wrapped phase data, (b) unwrapping path, (c) quality map, (d) unwrapped phase data (Zhao et al, 2011).

As indicated by Zhao et al (2011), the pixels can be unwrapped by following the line of coding in equation 16.

$$\varphi_a^u = \varphi_a^w + 2\pi * \text{round} \left(\frac{\varphi_b^u - \varphi_a^w}{2\pi} \right) \quad (16)$$

Where:

a and b are neighboring pixels, where b is unwrapped and a is wrapped.

The round() function returns the input as the nearest integer.

φ_b^u is the unwrapped phase of a pixel b.

φ_a^w is the wrapped phase of a pixel a.

φ_a^u is the unwrapped phase of a pixel a.

However, some problems arise from using this method, mainly, the presence of noise can result in wrong unwrapped phase values; invalid areas caused, for example, by shadows over the captured image of the object may propagate errors into other pixels; discontinuities aren't detected by this method and thus considered continuous, resulting in incorrect unwrapping; if for any of the mentioned reasons, a pixel is wrongly unwrapped, the next pixels who are unwrapped based on the wrongly unwrapped pixel will also be wrong (Zhao et al, 2011).

In Figure 21, a simple representation of how the unwrapping process based on unwrapped neighboring pixels functions, can be observed. As per Figure 21, when it comes to unwrapping the pink pixels, the quality map is considered and the highest quality pixels are unwrapped first, while the low-quality pixels, such as pixels affected by noise, are unwrapped last (Zhao et al, 2011). This is done to avoid incorrectly unwrapping a pixel, resulting in an error that might propagate.

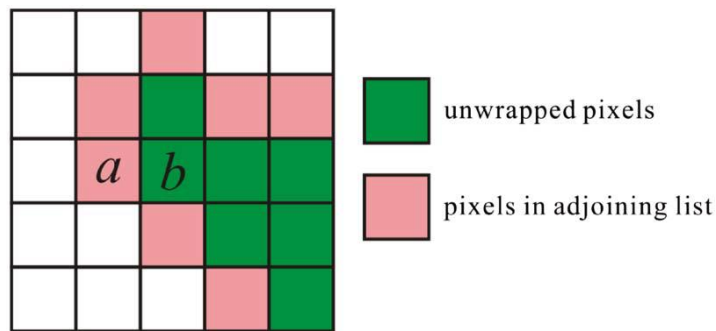


Figure 21 - Representation of spatial unwrapping (Zhao et al, 2011).

Quality guided phase unwrapping methods is a subject that has been extensively developed, Asundi and Wensen (1998) presented a fast algorithm capable of attaining high accuracy by unwrapping different areas depending on their reliability, where highly reliable areas were processed first. Herráez *et al* (2002) proposed a two dimensional phase unwrapping algorithm that presented good results even in the presence of discontinuities or noise. Zhang *et al* (2007) presented in their paper a phase unwrapping algorithm for the three dimensional measurement of shapes, this algorithm was tested on human faces, where data containing normal human expressions was unwrapped correctly 99% of the time, as for exaggerated facial expressions, the algorithm unwrapped the data correctly 97% of the time, as opposed to a fast line scanning unwrapping algorithm that failed almost 87% of the time. Wang *et al* (2011) developed and presented a three-dimensional quality-guided phase unwrapping method that when compared with a sequential quality unwrapping method, proved to be more robust.

4. System validation

The following section aims to fulfill the two final objectives proposed in subsection 1.2, the assembly of the Single-shot deflectometry system and its testing. To this end, the previously described monoscopic setup was implemented as described in subsection 3.1 using the hardware and auxiliary printed components introduced in subsection 3.2. Utilizing the described methods for demodulating and phase unwrapping in subsection 3.4 the newly written image post-processing algorithm was used to further test the captured images.

The subsections contained in this chapter will include an analysis of the setup implemented, the presentation of the object that will be used in the tests, the step-by-step execution of a Single-shot deflectometry system run and, finally, the selection and capture of two different surface images of the object to be evaluated and their post-processing. Finally, the obtained results are displayed and subsequently briefly discussed.

4.1. System setup and calibration

In Figure 22, the assembled Single-shot deflectometry system is represented, where all the previously detailed components can be observed.

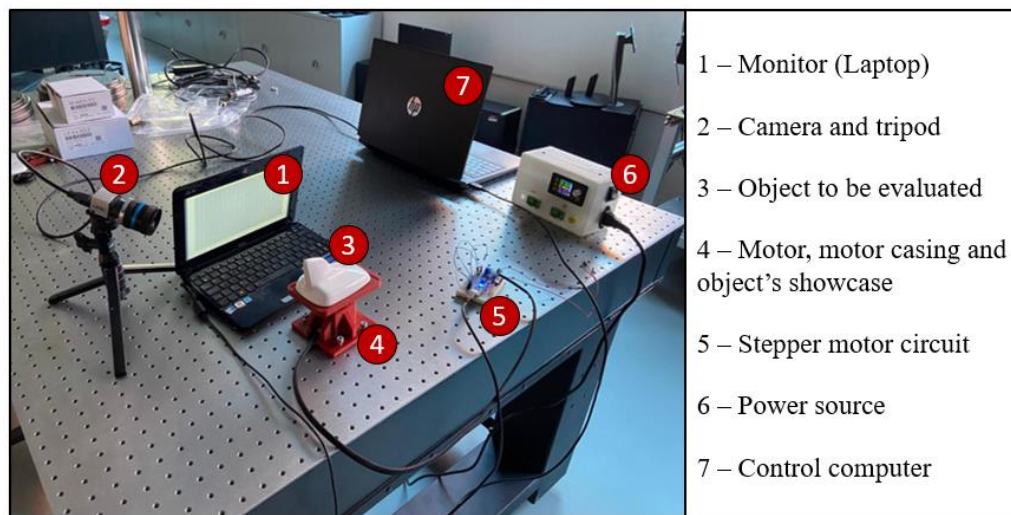


Figure 22 - Single-shot deflectometry system assembly.

Additionally, a power source deploying 12V and 2A was used to convey energy to the stepper motor. The electronic circuit powering the motor driver and the microcontroller as well as the CMOS camera were connected to a computer via USB.

Since no calibration technique was used, the correct positioning of the elements was assembled iteratively until the cross-fringe pattern was visible from the position of the camera and suitable results were obtained.

4.1.1. Object under test

It is important to fully grasp the geometry of the object that will be used to test the Single-shot deflectometry system. The object is hollow, contains a base on which it can be supported, leaving its upper surface to be tested, its geometry is complex and the external surface is highly reflective, which is difficult to handle with alternative techniques. A comprehensive visual representation of this component can be found in Figure 23.



Figure 23 - Object to be evaluated.

Two major different surface areas can be identified in the test object, as is visible in Figure 24. Surface A is the object's surface area somewhat parallel to its base, and surface B consists of a protrusion from surface A. While in Figure 24 only one side of the protrusion is highlighted in blue, for convenience, its opposite side must also be available for evaluation. Several objects of this exact geometry are available for testing, and these two surfaces cover all the surface defects presented.

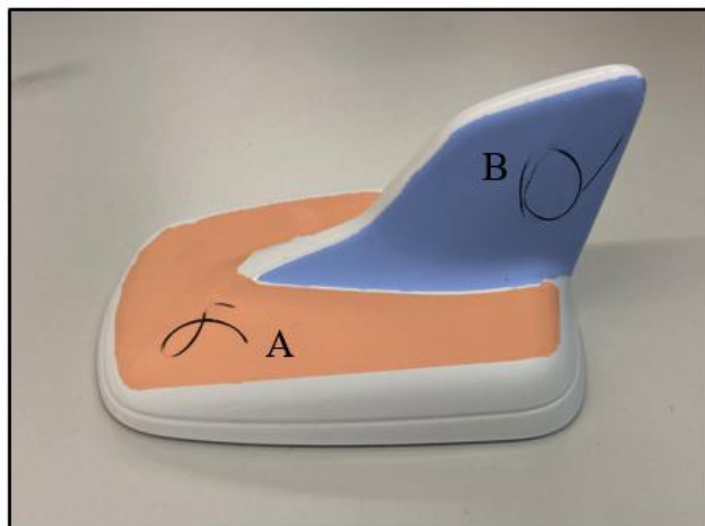


Figure 24 - Object's main areas of interest.

As for the example used and observable in Figure 24, the black line on the object's surface B outlines a surface defect while the black line in surface A indicates the type of defect that this object contains. Because this object possesses a complex curved surface shape, to evaluate its different surfaces, it is necessary to implement two slightly different system setups. Surface A demands the use of the motor incliners to clearly make visible the cross-fringe pattern reflected off it, while surface B doesn't require this auxiliary component.

4.2. Tests description

The description of the practical tests will use as an example the object displayed in Figure 23. The testing of this component includes the clear capture of the relevant image and its subsequent post-processing. This section will detail the various steps involved in these tests from the point of view of the user.

First, the object's area of interest must be identified, since photographing different areas of the object may imply a slightly different setup, as discussed before. For this example, the objective will be the successful identification of the defect present in area B of the object (Figure 24) which will not necessitate the integration of the motor incliners auxiliary component.

With the Single-shot deflectometry system in place as per Figure 22, the first step is to obtain the image of the area containing the surface defect while reflecting the cross-fringe pattern emitted from the laptop monitor. To this end, the user must simultaneously control the stepper motor by its firmware and search for a suitable image of the intended area containing the surface defect. The view of the object is obtained via the installed CMOS camera which the user then instructs to capture its image as soon as a suitable position displaying the relevant area is found. The captured image and objective for this first step can be observed in Figure 25.

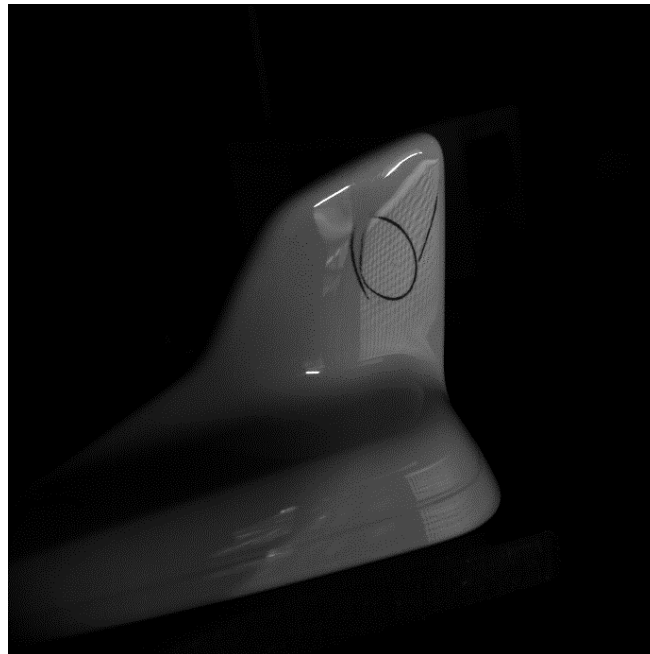


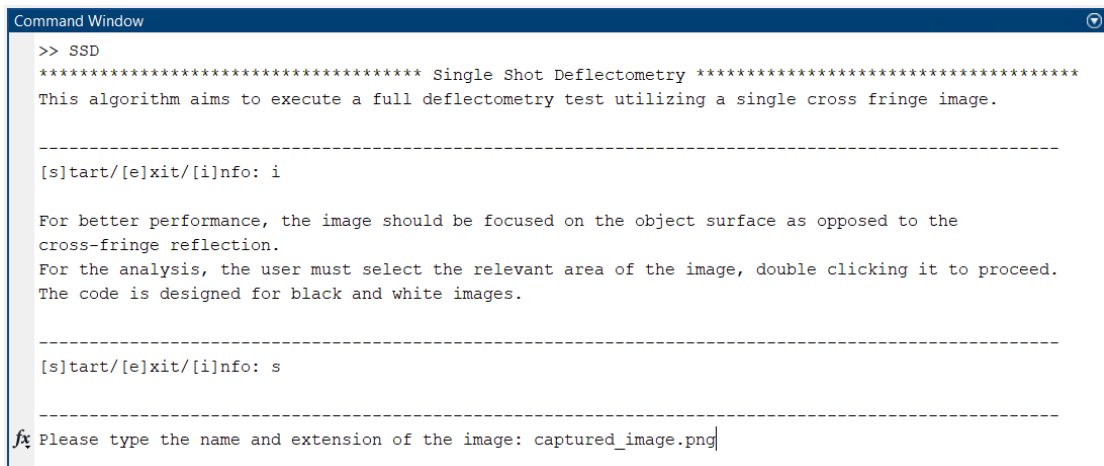
Figure 25 - Captured image of the object reflecting the cross-fringe pattern.

All the area containing the surface defect reflects the structured light pattern, the surrounding area is dark, and no shadows are placed upon the area that will be evaluated, therefore the correct precautions were implemented to avoid introducing errors in the post-processing stage and this picture is suitable to be used in the following steps.

The second step of this process initiates the image post-processing algorithm written in MATLAB and uploads the image to be processed. As soon as the algorithm is initiated, a small description of its intended purpose is provided, as well as the options to start the image processing, close the algorithm or to obtain further information by inserting the letters “s”, “e” or “i” respectively. If the user inserts the letter “i”, some important advice related to the image to be uploaded and the interface of the algorithm is presented. The advice regarding the image captured in the first step is substantiated by the research developed by Huang et al (2018), where it is stated that depending on what the camera is focusing on, results may vary. If the camera is focused on the surface of the object, the spatial resolution is very good, however, the angular resolution will decrease. The exact opposite happens when the camera is focused on the reflected cross-fringe image, achieving a decreased spatial resolution but higher angular resolution. Ultimately, in practical tests the camera is frequently focused on the surface of the

object since spatial resolution is an important requirement when it comes to three-dimensional shape measurement, also, the phase calculation of the sinusoidal patterns of the fringes, is not very sensitive to out-of-focus effects, as long as it is in a small amount and finally, when the camera focuses on the reflection instead of the object's surface, if a TFT LCD (Thin Film Transistor Liquid Crystal Display) is used, its pixel grids will be captured in the image, which may introduce errors in the image processing stage.

Afterwards, the algorithm presents the same three options, allowing the user to continue the image processing. Inserting "s" in the command window effectively starts that very same process, where the algorithm now requests the file name and extension of the image, this image must be located in the same working directory as the MATLAB algorithm. Figure 26 displays the initiating of the algorithm, the advice obtained by inserting "i" into the command window and the start of the image processing by pressing "s" and uploading the image.



```

Command Window
>> SSD
***** Single Shot Deflectometry *****
This algorithm aims to execute a full deflectometry test utilizing a single cross fringe image.

-----

[s]tart/[e]xit/[i]nfo: i

For better performance, the image should be focused on the object surface as opposed to the
cross-fringe reflection.
For the analysis, the user must select the relevant area of the image, double clicking it to proceed.
The code is designed for black and white images.

-----

[s]tart/[e]xit/[i]nfo: s

-----

fx Please type the name and extension of the image: captured_image.png

```

Figure 26 - Post-processing algorithm command window (MATLAB).

The third step starts as soon as the image obtained in the first step is uploaded. The user is now presented with the uploaded image and must select the area that will be processed by the algorithm (Figure 27).

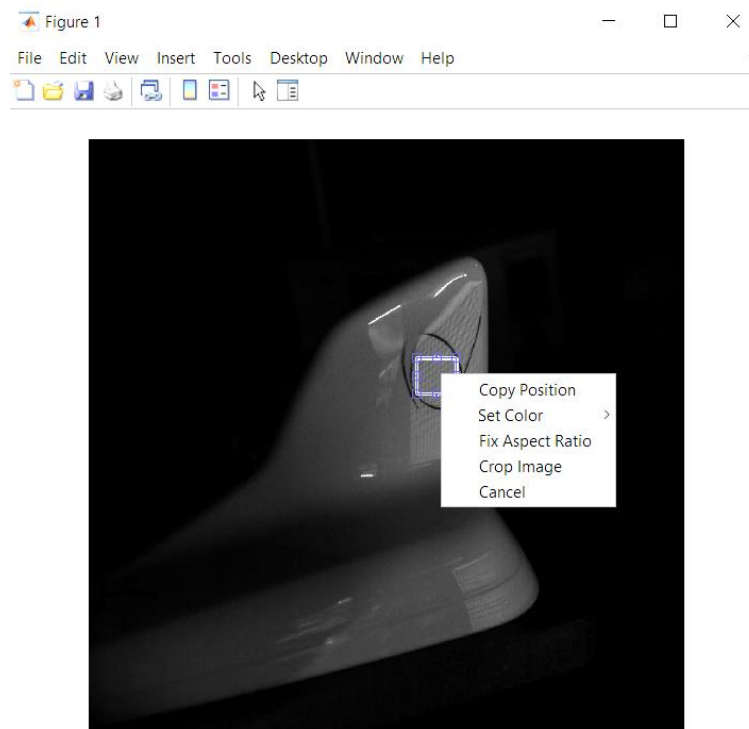


Figure 27 - Selection of the area to be processed by the algorithm (MATLAB).

This step enables a less strict photographing of the object since the relevant area to be analyzed can be specified in this part of the algorithm.

The user may select the area by clicking and dragging the mouse pointer, if a mistake is made, the area can be moved by once again clicking inside of its borders and dragging it, additionally, the user may resize the area by dragging any of its borders. To proceed, the user can either double click inside the selected area or right click and select "Crop Image". The selected area will then be cropped from this original image and be used for processing. In Figure 27, the uploaded image is displayed with the selection encompassing the surface area containing the defect.

The fourth step starts as soon as the image in step three is cropped, the algorithm starts to process the image, going through the methods described in Section 3 and eventually presenting the user with two more images. Both images represent the cropped image of the third step in the frequency domain, after its matrix is successfully shifted and the logarithmic operation is applied to it. In this map of frequencies, represented in Figure 28, two frequencies stand out, that correspond to the frequencies of the reflected vertical and horizontal cross-fringe pattern and, as described in Section 3, carry the information required to identify the surface defects.

Therefore, the user must now crop these frequencies manually, one per figure. In the first figure, the frequency of the horizontal fringes, which in this case is slightly tilted must be selected first, and the frequency related to the vertical fringes is selected afterwards, so that their respective phase images, wrapped and unwrapped, are correctly identified. Figure 28 displays both images, with the selected cropped areas.

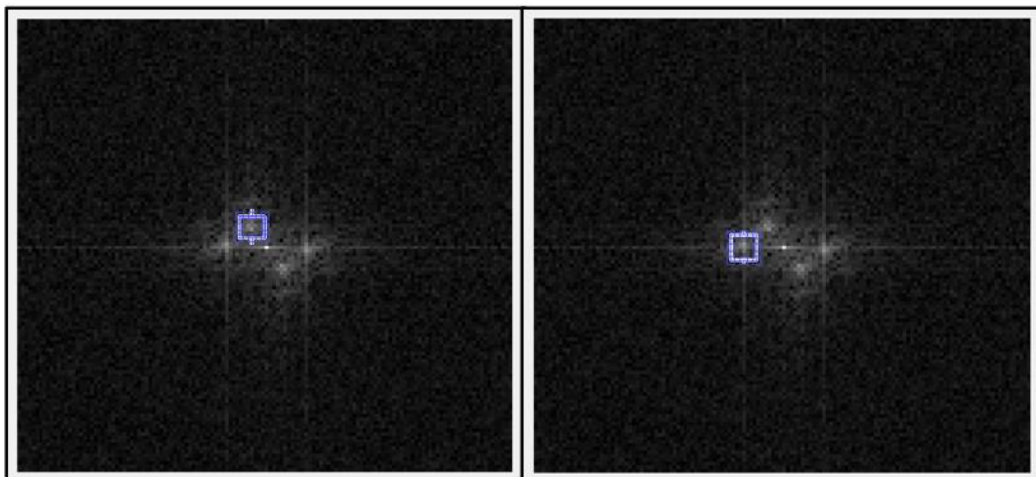


Figure 28 - Selection of the cross-fringe frequencies in the frequency domain (MATLAB).

Both cropped areas include the frequencies surrounding the main points of interest. In the following section, a small test will be applied to understand the influence of the cropped area on the final result. The user may now advance the same way as in the third step.

Finally, on what can be described as the fifth step, the results are presented. The user is now provided with a set of four images, for each of the fringes (vertical or horizontal), both the wrapped phase and unwrapped phase information is displayed. The wrapped phase information is displayed to identify possible problems on an unsuccessful test since the unwrapped phase data is the objective. These results can be found in Figure 29.

As is visible on both the unwrapped images, the surface defect is clearly visible and highlighted in Figure 29, however, results may differ depending on the selection made on the fourth step, as will be analyzed in the following subsection. The highlighted area represents the overall area where the defect is located on the image.

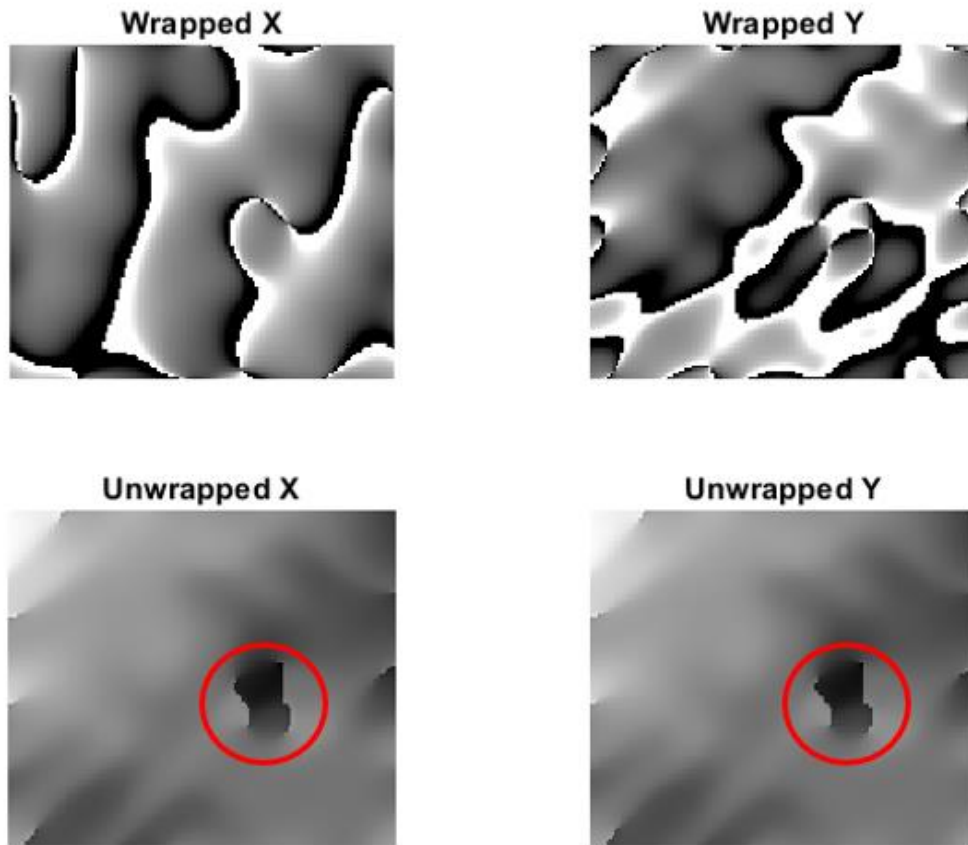


Figure 29 - Wrapped and unwrapped phase data (MATLAB).

4.3. Single-shot results

The test detailed in the previous subsection was taken into consideration, and following the same process, the practical test was applied to the very same object, however, in a region containing no defects in the surface to be analyzed. The captured image of this component is displayed in Figure 30.

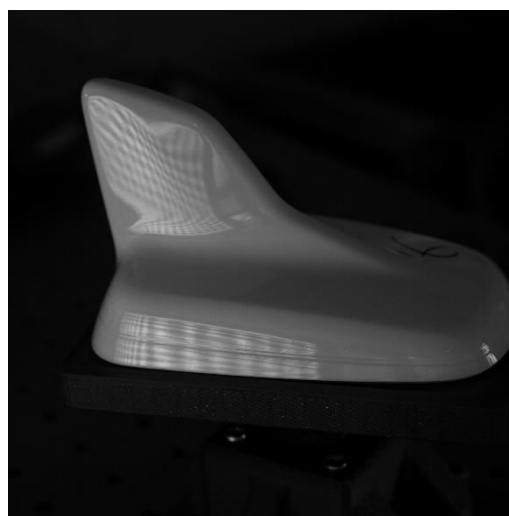


Figure 30 - Captured image of object without surface defect.

Furthermore, the compiled results of both tests, with and without a surface defect are presented in Figure 31. There, the unwrapped phase data for each image can be found.

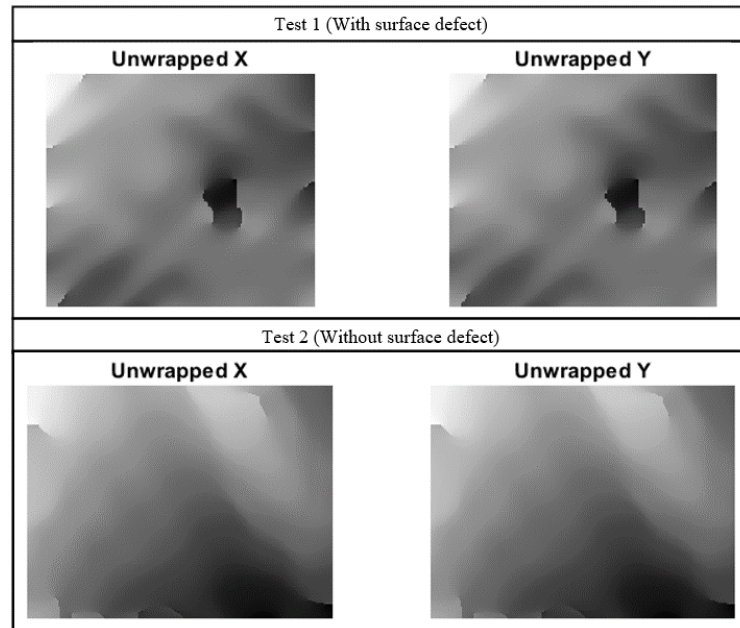


Figure 31 - Results of both tests (Unwrapped phase data).

Additionally, it is important to add that, for this method, the final result will vary depending on the crop window selected on the fourth step of the practical test, to see how this affects the result, several crop windows of differing size and position were applied and can be observed in Figure 32. Larger windows will include further frequencies and thereby increase resolution but may also introduce unnecessary noise.

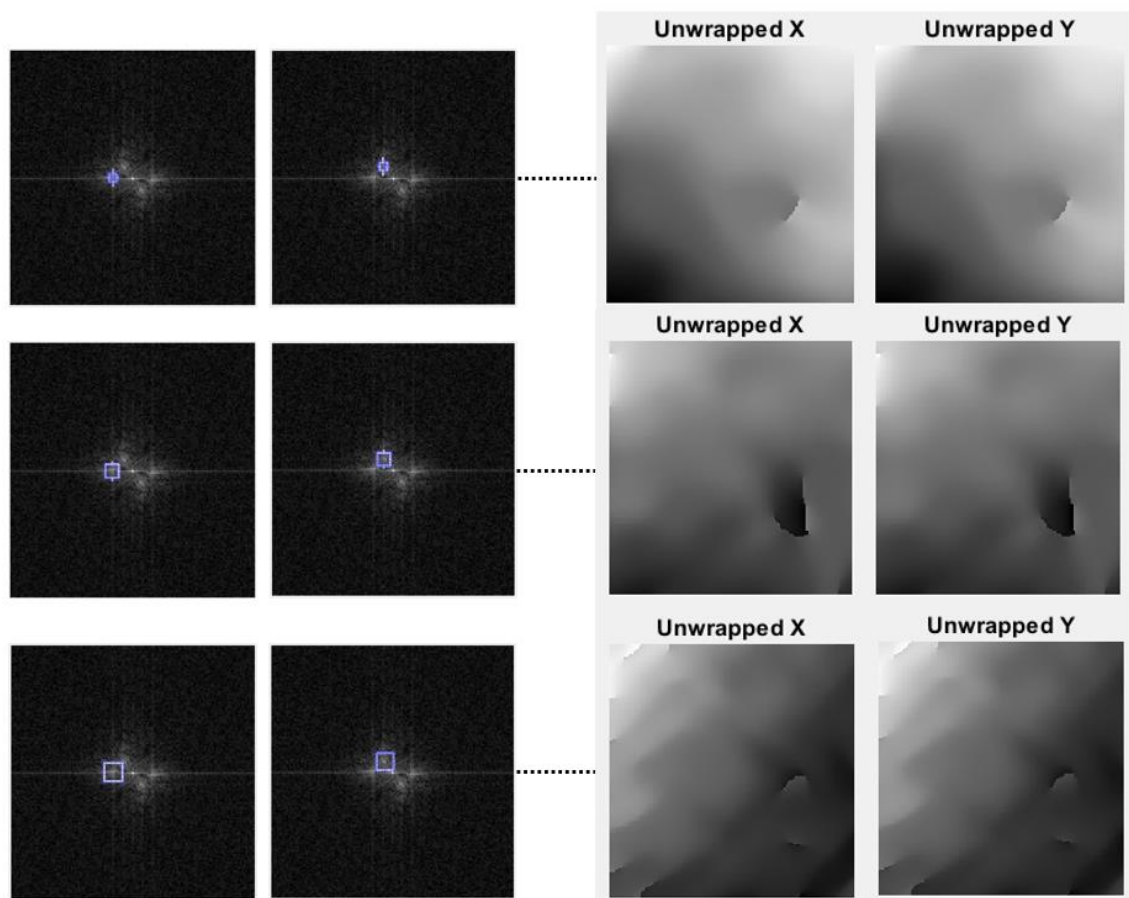


Figure 32 - Unwrapped phase data depending on the crop window.

It should be noted that the initial crop window applied in the second step may also influence the result, thus, for this type of testing, the same crop window is used for each example. The defect in surface B was chosen for this test since its analysis requires a setup with less components.

4.4. Brief discussion

The results obtained both in the system validation applied to the surface containing a defect and the surface without defects, as well as the results derived from the different crop windows are briefly addressed in this subsection.

The Single-shot deflectometry system itself can adapt to the type of surface area to evaluate and presents an adequate control of the angle of the object's position.

As is visible from the tests on the object with the defect on surface B, while one of the prominent points in the frequency domain belonged to the horizontal line crossing the center point, representing the vertical fringes, the other prominent point did not belong to the vertical line crossing the DC frequency point. This is because, as evidenced by the analysis done in subsection 3.4.1. (Figure 19), owing to the positioning of the components in the Single-shot deflectometry system, the horizontal fringes were captured in a tilted position by the camera. Nonetheless, the final unwrapped data of this test was able to display the surface defect clearly.

While the analysis of the surface containing no defects returned clean images for both unwrapped phase data, that is, displaying no surface defect as expected.

Thus, by observing and comparing both test results, it is possible to conclude that the system can produce adequate cross-fringe images of the object's surface, and that the post-processing algorithm produces adequate results that enable the correct identification of surface defects.

In addition, the final tests regarding the frequency domain crop selection have shown dependence on the size of the applied crop window. If a crop window is too small, not enough frequencies are processed and therefore, not enough information is captured for the final result, resulting in insufficient data that only represents the surface defect partially in the unwrapped phase data.

On the other hand, a very wide crop window captures too many frequencies, some of which may contain information related to the fringes in the other direction. The unwrapped phase data may not be able to present a suitable result, in this case. In the performed test, this resulted in the surface defect being barely visible, with only a few parts being noticeable.

One way to include bigger cropping windows without risking the last scenario is by using a cross-fringe pattern with a higher spatial resolution, this will allow the relevant frequencies to be further apart in the frequency domain, allowing for bigger crop windows without capturing frequencies relevant to the other fringes.

Another way to avoid this and allow a bigger crop window size is to make sure that the image contains the reflected cross-fringe pattern with its lines as close to the vertical and horizontal directions as possible, however, although this may be achieved in some cases by adjusting the camera or even the captured image (by rotating it), owing to the nature of the reflected pattern of light being deformed and the object's geometry, this may not always be feasible. In any case, if this is achieved, the relevant frequencies in the frequency domain will be in the lines that cross the DC frequency, one vertical and the other horizontal, therefore being located further apart than if one of the fringes were to be tilted in the captured image.

As such, when the user must crop the relevant frequencies in the frequency domain, that contain each the information of the vertical and horizontal fringes, respectively, caution must be exerted to not crop too much of the frequencies surrounding the relevant point, in turn capturing frequencies that contain information on the other fringes. However, the user must also be careful to not crop too little of the surrounding frequencies of a relevant point, capturing too little information to be processed instead, this may happen as a result to avoid cropping with a window that is too wide. In both cases, as seen before, the final unwrapped phase data will barely display any surface defects that are present.

In summary, when selecting the adequate crop window in step four of the post-processing algorithm, the user must select a window large enough to encompass the surrounding frequencies of a certain relevant point as much as possible, without approaching the crop window to another relevant point of frequency in the frequency domain. In the event that the results do not display the surface defect because of the applied crop window, the test must be reapplied from the beginning, which does not incur in severe time loss since the same image should already be stored in the same directory as the MATLAB algorithm.

If, despite a correct application of the crop window in step four, the final phase data does not display the surface defect, it is also possible that the picture is not suitable for post-processing. This method depends heavily on the quality of the captured image, which to be appropriate should not contain shadows and ideally most ambient light should be removed. The spatial frequency of the cross-fringe is also important, since if it is too low it might not be able to detect and correctly carry information regarding the surface defect.

5. Conclusion and future projects

5.1. Conclusion

The developed project has achieved all the goals that were proposed at the beginning of this dissertation.

A comprehensive state of the art analysis of non-destructive optical methods, with special consideration for PMD was performed and presented in this report. The entire mechanical solution of the Single-shot deflectometry system was successfully implemented by modelling and printing each component and integrate them with the hardware. The electronic solution of this project, encompassing the implementation of the electronic circuit used to control the stepper motor responsible for positioning the objects was also successfully done, as well as the required programming. As a result, all these components work together correctly in one single assembly. Finally, the image post-processing algorithm was rewritten, its methods changed to improve its functioning and the whole developed system, together with the post-processing algorithm was tested in a controlled environment.

Mechanically, the Single-shot deflectometry system is composed of a monitor, where a structured light cross-fringe image is displayed, the light from that monitor is reflected of the surface of the object and captured by a camera, that observes the structured light distorted, owing to the geometric shape and surface defects of the object under evaluation. Because the geometric shape of the object is challenging, it is necessary to tilt the object to be able to correctly capture certain surface areas. Overall, several three-dimensional printed components integrate this system, three to fix the stepper motor, encase it and display the object above it, allowing its rotation, and finally one to tilt the motor and the object, to capture certain areas of the objects surface.

Electronically, the computer gives instructions to the microcontroller via USB, and it communicates with the motor driver via UART communication and digital outputs. The main elements of the electronic circuit are therefore the microcontroller, Arduino NANO, and the stepper motor driver TMC2209. The control computer is thus able to send positioning commands to the motor, while visualizing the camera's point of view. The stepper motor's firmware was also developed, implementing its working regime of micro stepping, for better precision, and allowing it to rotate either 45°, 90°, 180° or 360°, depending on the user's input.

Since the original post-processing algorithm provided was not functioning correctly, a new improved version was written. The new post-processing algorithm aimed to present the unwrapped phase data as a final result, by demodulating and unwrapping the information carried in the captured image of the object's surface. The demodulation process was changed from the one used in the original algorithm, to the one described by Tavares e Vaz (2006), which allowed the code to be more specific on which frequencies to process, thus improving the final result since the frequencies of the deformed cross-fringe light pattern which carry the relevant information for the surface of the object could be selected more precisely. In contrast, the previous algorithm only applied a pre-defined mask to the images, which, depending on its thickness and the cross-fringe tilt, may produce incorrect results. The phase unwrapping technique was adapted from an algorithm described by Kemaio (2007), since it was compatible with the results obtained from the described demodulation method.

While this demodulation method has the potential to be more precise than the previous one, it also requires user input. The user must select the relevant frequency points and its surrounding frequencies carefully so not to capture frequencies belonging to other relevant points.

To make the user input's contribution easier to execute, some steps may be taken such as, make sure the cross-fringe fringes are as close to horizontal or vertical as possible in the captured image, this can be done by altering the setup slightly, and by using a cross-fringe image with a higher spatial resolution.

Finally, the Single-shot deflectometry system was tested under a controlled environment where an image containing a surface defect and another without surface defects were taken and then processed by the algorithm and compared. The algorithm was able to correctly display that on one image there existed a surface defect, and on the other no surface defect was detected. It

should be noted that the type of defects that this system aims to identify correspond to disturbances on the SUT caused by problems during the object's manufacture. These defects can occupy a small area, such as indents, or be correlated to a bigger, gradual surface deformation which is harder to detect.

Overall, the system can easily maneuver the object to expose its surface to the camera, although low ambient light is required to minimize interference in the captured image. Additionally, no shadows should be present in the object's surface to prevent errors in the post-processing phase and the spatial frequency of the fringe patterns must be high enough for the defects to be visible. The electronic part of the system works correctly and the post-processing algorithm, provided with a suitable image and careful user input, can clearly display the surface defects of the object's surface. Therefore, the developed system can detect surface defects based on a single cross-fringe image, making it ideal for dynamic applications in the area of quality control.

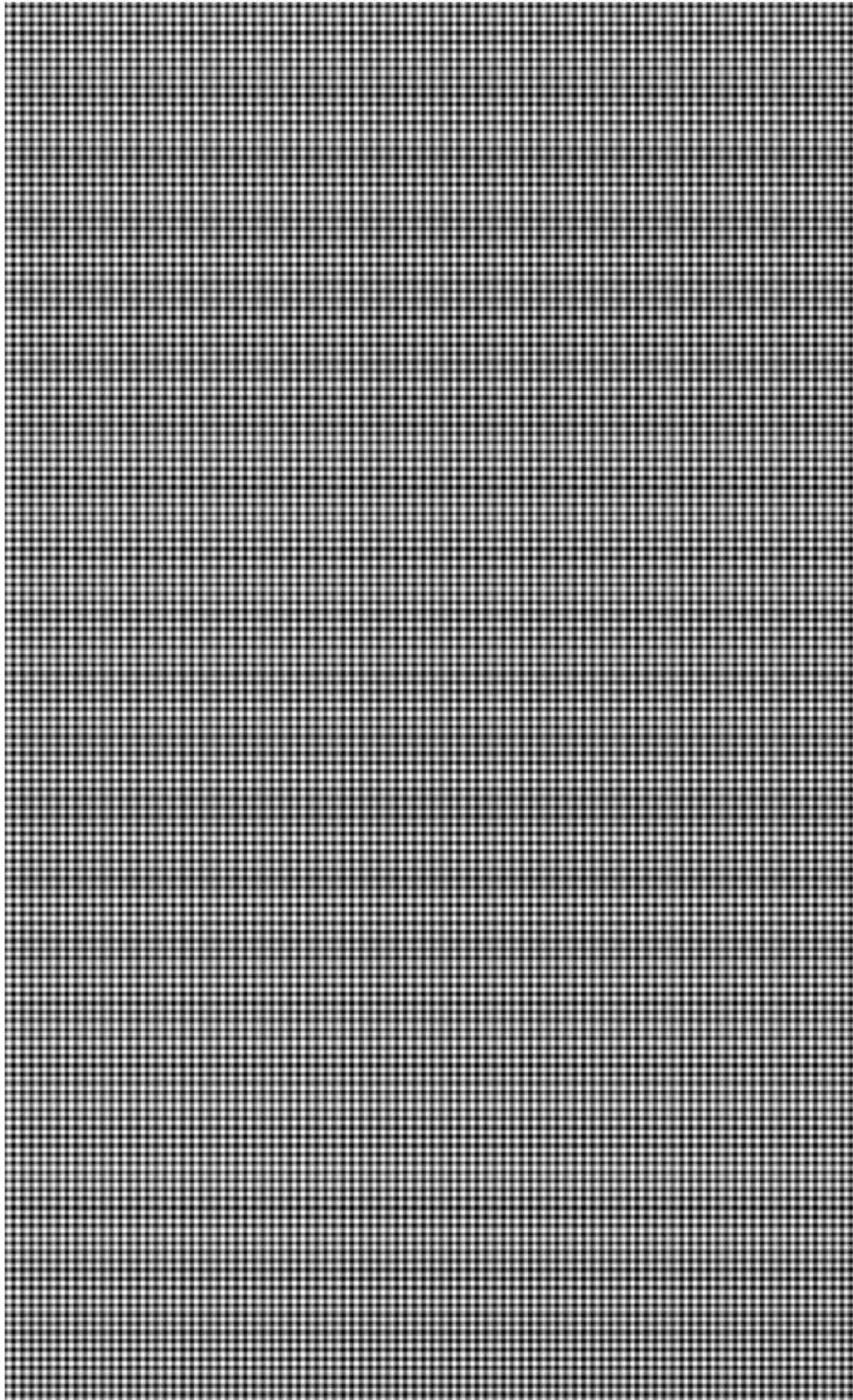
5.2. Future projects

The project developed during the writing of this paper can be used to further improve a more complete version of this prototype in the future. In this final subsection some suggestions to improve this deflectometry system in future iterations are presented:

- Combine the final phase data results of each of both the horizontal and vertical fringes into a single phase data image of the object's surface;
- 3D reconstruction of the object's surface, which implies a more detailed geometry and camera calibration;
- A more complete object movement system, with a higher degree of freedom of rotation, as opposed to a single rotation axis. This may be achieved, for example, by employing a robotized arm carrying both a camera and display;
- Develop a method for selecting the Fourier domain windows without user input.

Annexes

Annex A: Cross-fringe pattern



Annex B: IDS Camera data sheet (IDS Imaging Development Systems GmbH, n.d.)



UI-3370CP-M-GL Rev.2 (AB00519)



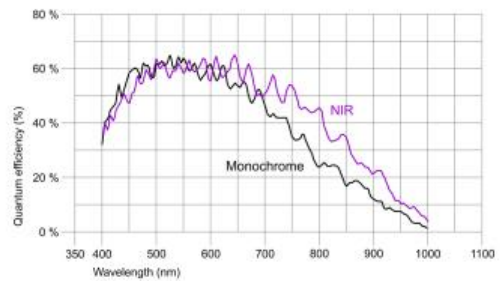
Discontinued
The model has been discontinued.



IDS peak uEye industrial cameras now also work with IDS peak! We recommend the Software Development Kit for the implementation of new projects. [Learn about the process here and switch now.](#)
Please note: The technical data given here was measured using the IDS Software Suite.

Specification

Sensor	
Sensor type	CMOS Mono
Shutter	Global Shutter
Sensor characteristic	Linear
Readout mode	Progressive scan
Pixel Class	4 MP
Resolution	4.19 Mpix
Resolution (h x v)	2048 x 2048 Pixel
Aspect ratio	1:1
ADC	12 bit
Color depth (camera)	12 bit
Optical sensor class	1"
Optical Size	11.264 mm x 11.264 mm
Optical sensor diagonal	15.93 mm (1/1")
Pixel size	5.5 µm
Manufacturer	ams/CMOSIS
Sensor Model	CMV4000-3E5M
Gain (master/RGB)	4x/-
AOI horizontal	same frame rate
AOI vertical	increased frame rate
AOI image width / step width	16 / 4
AOI image height / step width	2 / 2
AOI position grid (horizontal/vertical)	2 / 2
Binning horizontal	-
Binning vertical	-
Binning method	-
Binning factor	-
Subsampling horizontal	same frame rate
Subsampling vertical	increased frame rate
Subsampling method	M/C automatic
Subsampling factor	2, 4, 6, 8



Subject to technical modifications (2022-06-28)

Page 1 of 2

www.ids-imaging.com

IDS Imaging Development Systems GmbH
Dimbacher Str. 10 · 74182 Obersulm · Germany · Phone +49 7134 96196-0 · E-mail info@ids-imaging.com



UI-3370CP-M-GL Rev.2 (AB00519)

Model

Pixel clock range	38 MHz - 344 MHz
Frame rate freerun mode	80
Frame rate trigger (maximum)	80
Exposure time (minimum - maximum)	0.038 ms - 500 ms
Power consumption	1.8 W - 3.6 W
Image memory	128 MB
Special features	Overlap trigger, Dual exposure, Sensor source gain, Multi-AOI

Ambient conditions

The temperature values given below refer to the outer device temperature of the camera housing.

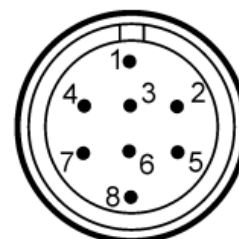
Device temperature during operation	0 °C - 55 °C / 32 °F - 131 °F
Device temperature during storage	-20 °C - 60 °C / -4 °F - 140 °F
Humidity (relative, non-condensing)	20 % - 80 %

Connectors

Interface connector	USB 3.0 micro-B, screwable
I/O connector	8-pin Hirose connector (HR25-7TR-8PA(73))
Power supply	USB cable

Pin assignment I/O connector

1	Ground (GND)
2	Flash output with optocoupler (-)
3	General Purpose I/O (GPIO) 1
4	Trigger input with optocoupler (-)
5	Flash output with optocoupler (+)
6	General Purpose I/O (GPIO) 2
7	Trigger input with optocoupler (+)
8	Output supply voltage, 5 V (100 mA)



Camera rear view

Design

Lens Mount	C-Mount
IP code	IP30
Dimensions H/W/L	29.0 mm x 29.0 mm x 29.0 mm
Mass	52 g

Subject to technical modifications (2022-06-28)

Page 2 of 2

www.ids-imaging.com

IDS Imaging Development Systems GmbH

Dimbacher Str. 10 · 74182 Obersulm · Germany · Phone +49 7134 96196-0 · E-mail info@ids-imaging.com

Annex C: Stepper motor list (Motion Control Products LTD, n.d.)

M42STH series- High Torque
42mm / NEMA Size 17, 1.8 degree

Hybrid Stepper Motors



General Specifications

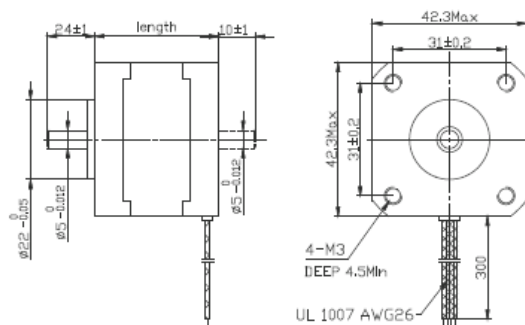
Step Angle Accuracy	±5% (full step, no load)
Resistance Accuracy	±10%
Inductance Accuracy	±20%
Temperature Rise	80°C max. (rated current, 2 phases on)
Ambient Temperature	-20°C ~ +50°C
Insulation Resistance	100MΩ min., 500VDC
Dielectric Strength	500VAC for one minute
Shaft Radial Play	0.02mm max. (450g load)
Shaft Axial Play	0.08mm max. (450g load)
Max. Radial Force	28N (20mm from the flange)
Max. Axial Force	10N

Model Specifications

Model Part Number		Voltage V	Current /phase A	Resistance /phase Ω	Inductance /phase mH	Holding Torque mNm	Rotor Inertia gcm ²	Detent Torque gcm	No. of Leads	Length mm	Weight g
Single shaft	Double shaft										
M42STH25-0404S	M42STH25-0404D	9.6	0.4	24	36	167	20	75	4	25	150
M42STH33-0956S	M42STH33-0956D	4	0.95	4.2	2.5	157	35	120	6	34	220
M42STH33-0406S	M42STH33-0406D	9.6	0.4	24	15	157	35	120	6	34	220
M42STH33-0316S	M42STH33-0316D	12	0.31	38.5	21	157	35	120	6	34	220
M42STH33-1334S	M42STH33-1334D	2.8	1.33	2.1	2.5	216	35	120	4	34	220
M42STH38-1206S	M42STH38-1206D	4	1.2	3.3	3.2	255	54	150	6	40	280
M42STH38-0806S	M42STH38-0806D	6	0.8	7.5	6.7	255	54	150	6	40	280
M42STH38-0406S	M42STH38-0406D	12	0.4	30	30	255	54	150	6	40	280
M42STH38-1684S	M42STH38-1684D	2.8	1.68	1.65	3.2	353	54	150	4	40	280
M42STH47-1206S	M42STH47-1206D	4	1.2	3.3	2.8	311	68	200	6	48	350
M42STH47-0806S	M42STH47-0806D	6	0.8	7.5	6.3	311	68	200	6	48	350
M42STH47-0406S	M42STH47-0406D	12	0.4	30	25	311	68	200	6	48	350
M42STH47-1684S	M42STH47-1684D	2.8	1.68	1.65	2.8	431	68	200	4	48	350
M42STH60-1206S	M42STH60-1206D	7.2	1.2	6	7	637	102	280	6	60	500

Page

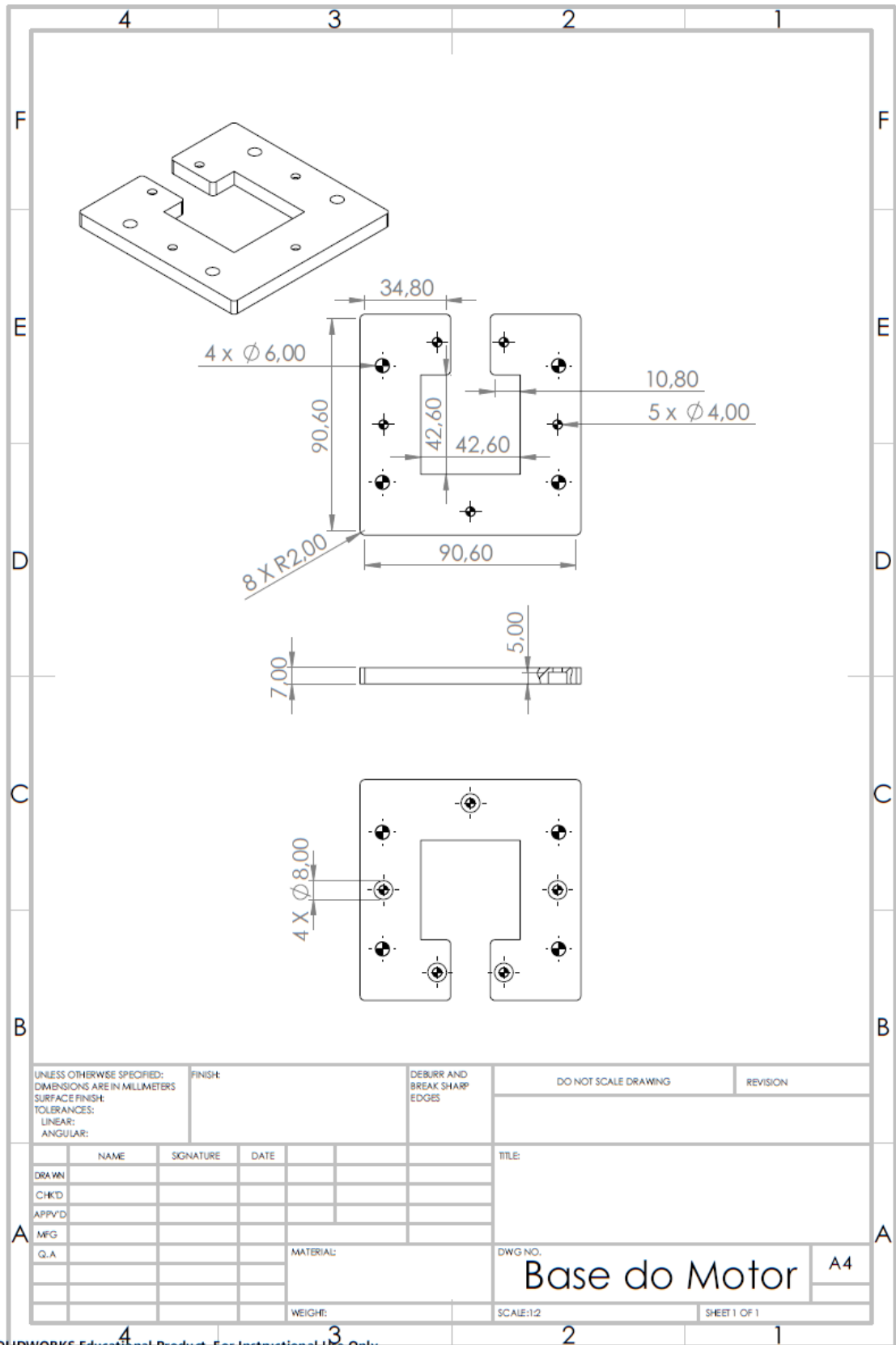
Dimensions (in mm)



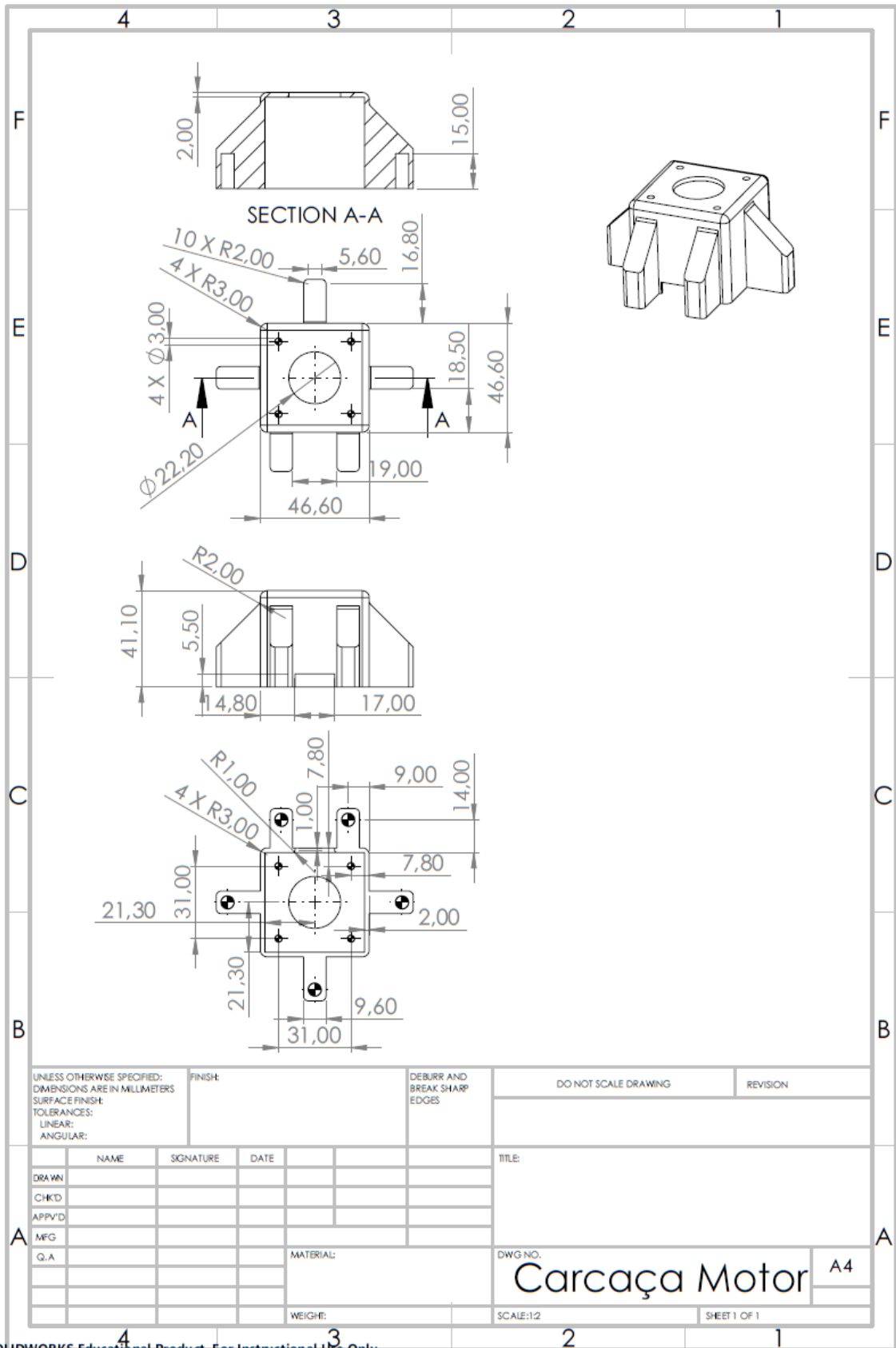
Connections



Annex D: Stepper motor base technical drawing

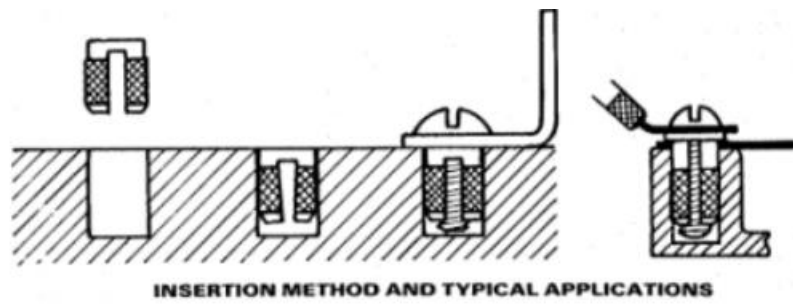


Annex E: Stepper motor casing technical drawing



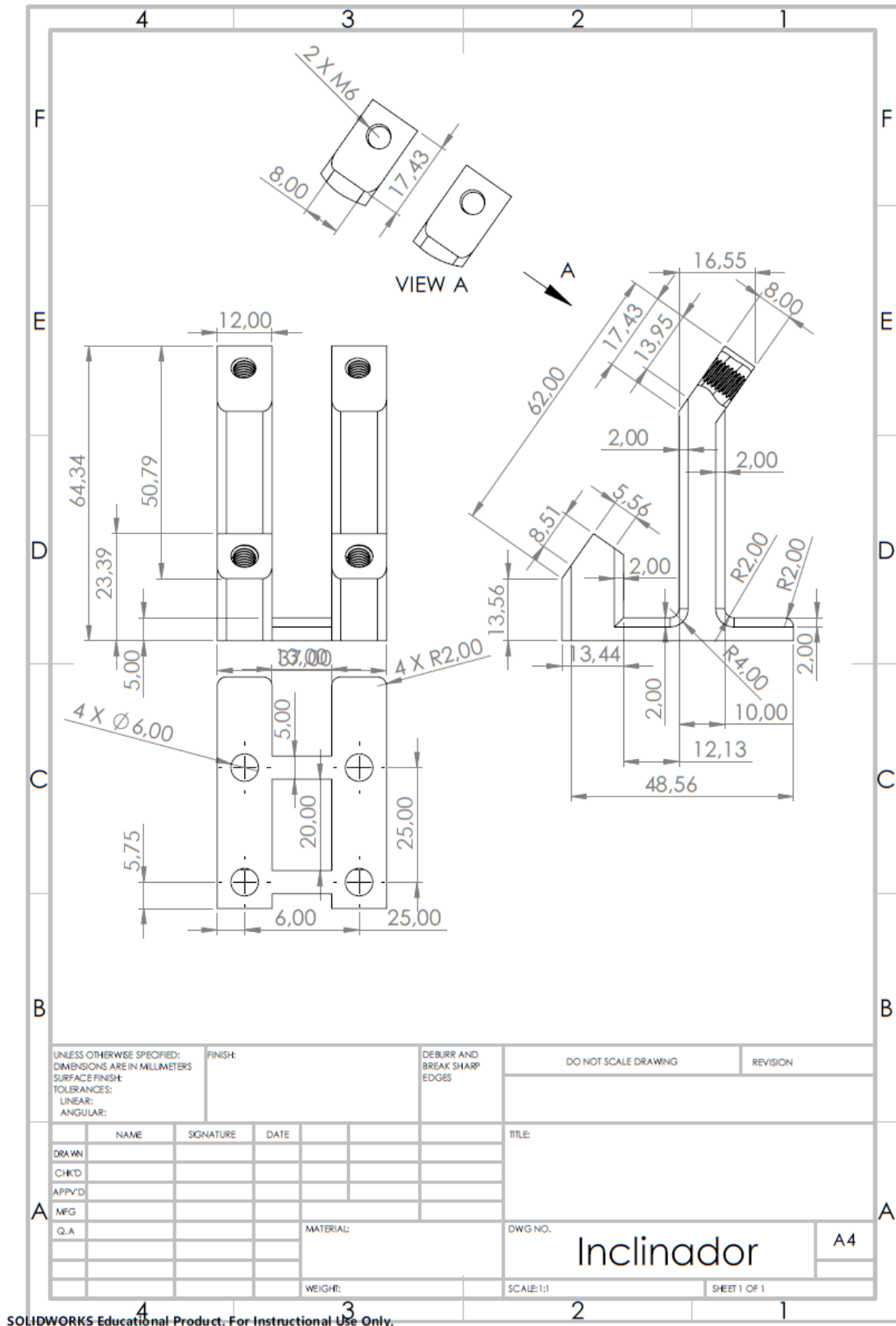
SOLIDWORKS Educational Product. For Instructional Use Only.

Annex F: M4 brass threaded inserts specifications (RS Pro, n.d.)



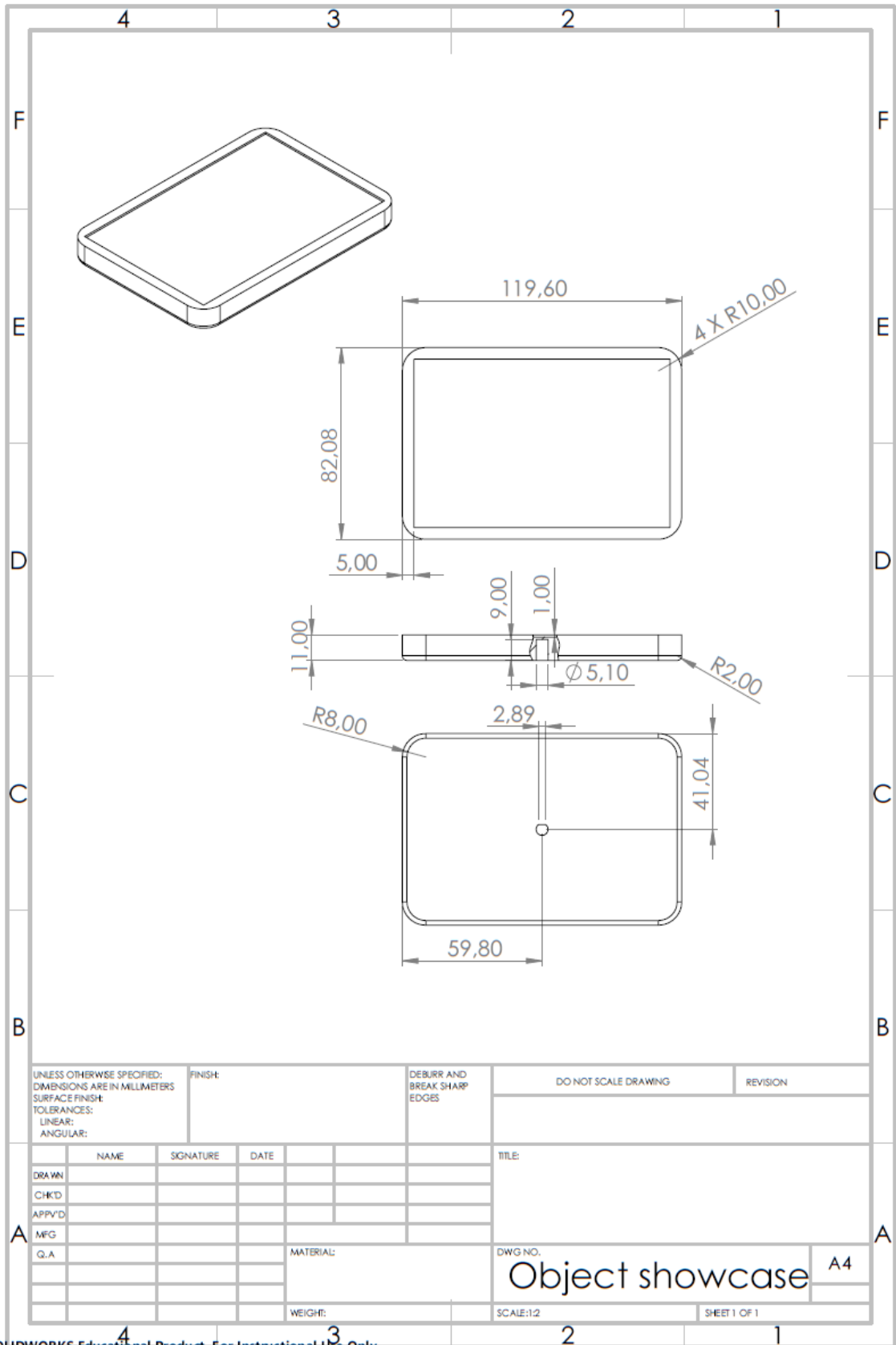
Stock No.	Material	Thread Size	Fixing Hole Diameter	Body Outside Diameter	Body Depth	Thickness of Material Minimum	Mounting Depth
278-534	Brass	M3	4 mm	4.22 mm	4.78mm	6.7 mm	Flush
278-540	Brass	M3.5	4.8 mm	5.06 mm	6.35mm	8.4 mm	Flush
278-556	Brass	M4	5.6 mm	5.64 mm	7.95mm	10.2 mm	Flush
278-562	Brass	M5	6.4 mm	6.65 mm	9.35mm	12.2 mm	Flush
278-578	Brass	M6	8 mm	8.26 mm	12.7mm	16 mm	Flush
278-584	Brass	M3	4 mm	4.22 mm	4.78mm	6.2 mm	Flush
278-590	Brass	M3.5	4.8 mm	5.06 mm	6.35mm	7.8 mm	Flush
278-607	Brass	M4	5.6 mm	5.64 mm	7.95mm	9.4 mm	Flush
278-613	Brass	M5	6.4 mm	6.65 mm	9.53mm	11.2 mm	Flush
278-629	Brass	M6	8 mm	8.26 mm	12.7mm	14.8 mm	Flush

Annex G: Motor inliner technical drawing



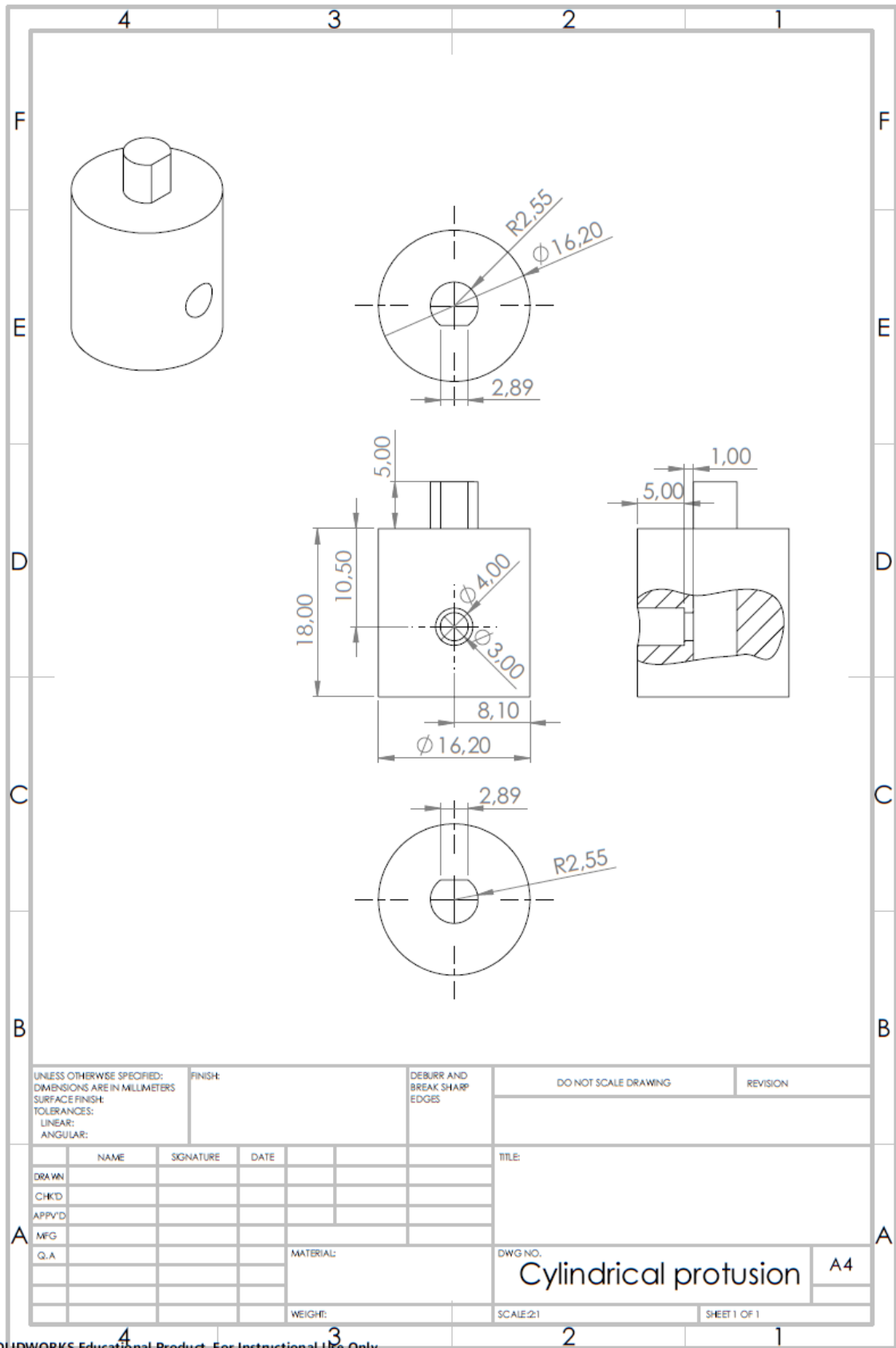
SOLIDWORKS Educational Product. For Instructional Use Only.

Annex H: Object stand technical drawing

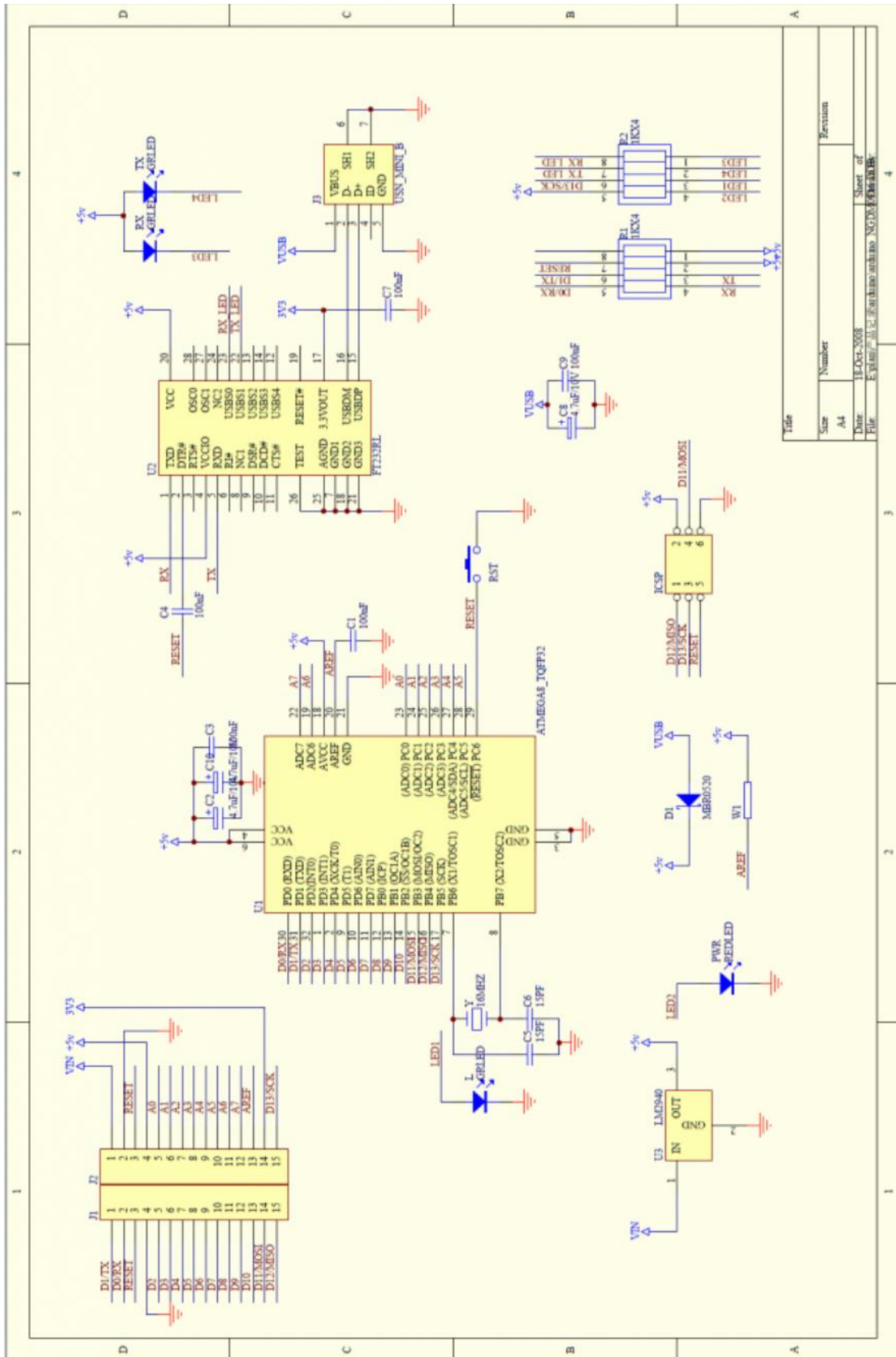


SOLIDWORKS Educational Product. For Instructional Use Only.

Annex I: Cylindrical protrusion technical drawing



Annex J: Arduino NANO electrical connections (HK Shan Hai Group Limited, n.d.)



Annex K: Stepper motor firmware

```

#include <TMCStepper.h>
#include <SoftwareSerial.h>

SoftwareSerial tmc2209Serial(6,7); //(RX,TX)

#define EN_PIN          12
#define DIR_PIN         8
#define STEP_PIN        9
#define SW_RX           6
#define SW_TX           7
#define SERIAL_PORT     tmc2209Serial
#define DRIVER_ADDRESS  0b00
#define R_SENSE         0.11f

TMC2209Stepper driver(&SERIAL_PORT, R_SENSE, DRIVER_ADDRESS);

int user_input;

void setup() {
  Serial.begin(9600);
  SERIAL_PORT.begin(115200);
  driver.beginSerial(115200);

  pinMode(EN_PIN, OUTPUT);
  pinMode(STEP_PIN, OUTPUT);
  pinMode(DIR_PIN, OUTPUT);
  digitalWrite(EN_PIN, LOW);

  driver.begin();
  driver.toff(5);
  driver.rms_current(600);
  driver.microsteps(16);
}

void loop() {
  Serial.println("Please input one of the following
options:");
  Serial.println("      1: Rotates study object by 45°");

```

```
Serial.println("    2: Rotates study object by 90°");
Serial.println("    3: Rotates study object by 180°");
Serial.println("    4: Rotates study object by 360°");
Serial.println(" ");
Serial.println("(Clockwise rotations)");

while (Serial.available() == 0){
    //Waiting for user to input data
}
user_input = Serial.parseInt();

if (user_input == 1){
    for (uint16_t i = 400; i>0; i--){
        digitalWrite(STEP_PIN, HIGH);
        delayMicroseconds(640);
        digitalWrite(STEP_PIN, LOW);
        delayMicroseconds(640);
    }
} else if (user_input == 2){
    for (uint16_t i = 800; i>0; i--){
        digitalWrite(STEP_PIN, HIGH);
        delayMicroseconds(640);
        digitalWrite(STEP_PIN, LOW);
        delayMicroseconds(640);
    }
} else if (user_input == 3){
    for (uint16_t i = 1600; i>0; i--){
        digitalWrite(STEP_PIN, HIGH);
        delayMicroseconds(640);
        digitalWrite(STEP_PIN, LOW);
        delayMicroseconds(640);
    }
} else if (user_input == 4){
    for (uint16_t i = 3200; i>0; i--){
        digitalWrite(STEP_PIN, HIGH);
        delayMicroseconds(640);
        digitalWrite(STEP_PIN, LOW);
        delayMicroseconds(640);
    }
}
```

```
    }  
}  
  
    Serial.println("The study object has been rotated.");  
    Serial.  
println("-----");  
}
```

References

- Akhtar, S., A. Tandiya, M. Moussa and C. Tarry (2019). "An Efficient Automotive Paint Defect Detection System." *Advances in Science, Technology and Engineering Systems Journal* 4(3): 171-182.
- Asundi, A. and Z. Wensen (1998). "Fast phase-unwrapping algorithm based on a gray-scale mask and flood fill." *Applied optics* 37(23): 5416-5420.
- Biqu. n.d. "BTT TMC2209 V1.2 UART Stepper Motor Driver | Biqu Equipment". Accessed July 3, 2022. <https://biqu.equipment/products/bigtreotech-tmc2209-stepper-motor-driver-for-3d-printer-board-vs-tmc2208>
- Fisher, R., Perkins, S., Walker, A. and Wolfart, E. 2003. "Image Transforms – Fourier Transform.". Accessed July 21, 2022. <https://homepages.inf.ed.ac.uk/rbf/HIPR2/fourier.htm>
- Fisher, R., S. Perkins, A. Walker and E. Wolfart (1996). "Hypermedia image processing reference." England: John Wiley & Sons Ltd: 118-130.
- Ghiglia, D. C. and M. D. Pritt (1998). "Two-dimensional phase unwrapping: theory, algorithms, and software." A Wiley Interscience Publication.
- Groot, P. d. (2011). *Phase shifting interferometry. Optical measurement of surface topography*, Springer: 167-186.
- Herráez, M. A., D. R. Burton, M. J. Lalor and M. A. Gdeisat (2002). "Fast two-dimensional phase-unwrapping algorithm based on sorting by reliability following a noncontinuous path." *Applied optics* 41(35): 7437-7444.
- HK Shan Hai Group Limited. n.d. "Nano V3".
- Horneber, C., M. Knauer and G. Häusler (2000). "Phase Measuring Deflectometry: a new method to measure reflecting surfaces." annual report, Lehrstuhl für Optik, University of Erlangen-Nuremberg.
- Huang, L., M. Idir, C. Zuo and A. Asundi (2018). "Review of phase measuring deflectometry." *Optics and Lasers in Engineering* 107: 247-257.
- Huke, P., J. Burke and R. B. Bergmann (2014). A comparative study between deflectometry and shearography for detection of subsurface defects. *Interferometry XVII: Techniques and Analysis*, International Society for Optics and Photonics.
- IDS Imaging Development Systems GmbH. n.d. "UI-3370CP-M-GL Rev.2 (AB00519)". Accessed 28/06/2022.
- Ishikawa, K., T. Takamura, M. Xiao, S. Takahashi and K. Takamasu (2014). "Profile measurement of aspheric surfaces using scanning deflectometry and rotating autocollimator with wide measuring range." *Measurement Science and Technology* 25(6): 064008.
- Kemao, Q. (2007). "Two-dimensional windowed Fourier transform for fringe pattern analysis: principles, applications and implementations." *Optics and Lasers in Engineering* 45(2): 304-317.
- Kim, M. K. (2010). "Principles and techniques of digital holographic microscopy." *SPIE reviews* 1(1): 018005.
- Legarda-Saenz, R. (2007). "Robust wavefront estimation using multiple directional derivatives in moiré deflectometry." *Optics and lasers in engineering* 45(9): 915-921.
- Maldonado, A. V., P. Su and J. H. Burge (2014). "Development of a portable deflectometry system for high spatial resolution surface measurements." *Applied optics* 53(18): 4023-4032.
- Mazet, V. 2021. "Fourier Transform – Basics of Image Processing.". Accessed July 20, 2022. <https://vincmazet.github.io/bip/filtering/fourier.html>
- Motion Control Products LTD. n.d. "M42STH series- High Torque 42mm / NEMA Size 17, 1.8 degree".

- Palousek, D., M. Omasta, D. Koutny, J. Bednar, T. Koutecky and F. Dokoupil (2015). "Effect of matte coating on 3D optical measurement accuracy." *Optical Materials* 40: 1-9.
- Royo, S. (1999). Topographic measurements of non-rotationally symmetrical concave surfaces using Ronchi deflectometry, Universitat Politècnica de Catalunya.
- RS Pro. n.d. "RS PRO, M4 Brass Threaded Insert diameter 5.6mm Depth 7.95mm".
- Salvi, J., X. Armangué and J. Batlle (2002). "A comparative review of camera calibrating methods with accuracy evaluation." *Pattern recognition* 35(7): 1617-1635.
- Sansoni, G., M. Trebeschi and F. Docchio (2009). "State-of-the-art and applications of 3D imaging sensors in industry, cultural heritage, medicine, and criminal investigation." *Sensors* 9(1): 568-601.
- Schatzman, J. C. (1996). "Accuracy of the discrete Fourier transform and the fast Fourier transform." *SIAM Journal on Scientific Computing* 17(5): 1150-1166.
- Tavares, P. J. (2008). Three-dimensional geometry characterization using structured light fields, Universidade do Porto (Portugal).
- Tavares, P. J. and M. A. Vaz (2006). "Orthogonal projection technique for resolution enhancement of the Fourier transform fringe analysis method." *Optics Communications* 266(2): 465-468.
- Tavares, P. J. and M. A. Vaz (2013). "Single image orthogonal fringe technique for resolution enhancement of the fourier transform fringe analysis method." *Optics Communications* 290: 33-36.
- Tiziani, H. J. and H. M. Uhde (1994). "Three-dimensional image sensing by chromatic confocal microscopy." *Applied optics* 33(10): 1838-1843.
- Tsai, R. (1987). "A versatile camera calibration technique for high-accuracy 3D machine vision metrology using off-the-shelf TV cameras and lenses." *IEEE Journal on Robotics and Automation* 3(4): 323-344.
- Wang, B., X. Luo, T. Pfeifer and H. Mischo (1999). "Moire deflectometry based on Fourier-transform analysis." *Measurement* 25(4): 249-253.
- Wang, C., J. Kim, C. T. Jin, P. H. Leong and A. McEwan (2012). "Near infrared spectroscopy in optical coherence tomography." *Journal of near infrared spectroscopy* 20(1): 237-247.
- Wang, H., J. B. Weaver, I. I. Perreard, M. M. Doyley and K. D. Paulsen (2011). "A three-dimensional quality-guided phase unwrapping method for MR elastography." *Physics in Medicine & Biology* 56(13): 3935.
- Xu, J., P. Wang, Y. Yao, S. Liu and G. Zhang (2017). "3D multi-directional sensor with pyramid mirror and structured light." *Optics and Lasers in Engineering* 93: 156-163.
- Zhang, S., X. Li and S.-T. Yau (2007). "Multilevel quality-guided phase unwrapping algorithm for real-time three-dimensional shape reconstruction." *Applied optics* 46(1): 50-57.
- Zhang, Z. (2000). "A flexible new technique for camera calibration." *IEEE Transactions on pattern analysis and machine intelligence* 22(11): 1330-1334.
- Zhang, Z., Y. Wang, S. Huang, Y. Liu, C. Chang, F. Gao and X. Jiang (2017). "Three-dimensional shape measurements of specular objects using phase-measuring deflectometry." *Sensors* 17(12): 2835.
- Zhao, M., L. Huang, Q. Zhang, X. Su, A. Asundi and Q. Kemao (2011). "Quality-guided phase unwrapping technique: comparison of quality maps and guiding strategies." *Applied optics* 50(33): 6214-6224.